Title: Direct activation of NADPH oxidase 2 by 2-deoxyribose-1-phosphate triggers nuclear factor kappa B-dependent angiogenesis

Short title: NOX2-dependent angiogenesis

Authors: Dina Vara[1], Joanna M ~~Swarbrick~~Watt[12], Tiago M Fortunato[13], Harry Mellor[42], Matthew Burgess[53], Kate Wicks[53], Kimberly Mace[53], Shaun Reeksting[64], Anneke Lubben[64], Caroline PD Wheeler-Jones[75] and Giordano Pula[1]*

[1]Institute of Biomedical and Clinical Science, University of Exeter Medical School, Exeter (UK); [2]D~~D~~epartment of Pharmacy and Pharmacology, University of Bath, Bath (UK); [3]Department of Biomedical Engineering, Eindhoven University of Technology, Eindhoven (The Netherlands) [24]Department of Biochemistry, University of Bristol, Bristol (UK); [5]The Healing Foundation Centre, University of Manchester, Manchester (UK); [6]Mass Spectrometry Service and Chemical Characterization and Analysis Facility, University of Bath, Bath (UK); [7]Department of Comparative Biomedical Sciences, Royal Veterinary College, London (UK).

*Corresponding author: Giordano Pula, Institute of Biomedical and Clinical Science, University of Exeter Medical School, Exeter EX1 2LU (UK), email: g.pula@exeter.ac.uk~~Department of Pharmacy and Pharmacology, University of Bath, Claverton Campus, Bath Spa (UK), BA2 7AY, Tel.: 0044(0)1225 386428, email: g.pula@bath.ac.uk~~.

Footnote: This work was presented in a reduced form at ESM-EVBO Conference 2017 (May 29 – June 2, Geneva, Switzerland) and the NADPH Oxidase Gordon Conference 2016 (June 5-10, Waterville US).

Manuscript keywords: NADPH, NOX, Angiogenesis, NF-kB, endothelial, ROS

Word count (excluding references and figure legends): ~~5685~~5864

Reference numbers: ~~69~~71

Formatted: Superscript

Formatted: Not Superscript/ Subscript

Number of greyscale illustrations: ~~12~~ 15 (7 hardcopy, ~~5~~ 8 online)

Number of color illustrations: 3 (3 hardcopy)

ABSTRACT

Aims: Deoxyribose-1-phosphate (dRP) is a pro-angiogenic paracrine stimulus released by cancer cells, platelets and macrophages and acting on endothelial cells. The objective of this study was to clarify how dRP stimulates angiogenic responses in human endothelial cells.

Results: Live cell imaging, electron paramagnetic resonance (EPR), pull-down of dRP-interacting proteins followed by immunoblotting, gene silencing of different NOXs and their regulatory co-subunits by siRNA transfection, and experiments with inhibitors of the sugar transporter GLUT1 were utilized to demonstrate that dRP acts intracellularly by directly activating the endothelial NADPH oxidase 2 (NOX2) complex, but not NOX4. Increased reactive oxygen species (ROS) generation in response to NOX2 activity leads to redox-dependent activation of the transcription factor nuclear factor kappa B (NF-κB), which, in turn, induces VEGF receptor 2 (VEGFR2) upregulation. Using endothelial tube formation assays, gene silencing by siRNA and antibody-based receptor inhibition, we demonstrate that the activation of NF-κB and VEGFR2 is necessary for the angiogenic responses elicited by dRP. The upregulation of VEGFR2 and the NOX2-dependent stimulation of angiogenesis by dRP was confirmed in excisional wound and matrigel plug vascularisation assays *in vivo* using $NOX2^{-/-}$ mice.

Innovation: For the first time, we demonstrate that dRP acts intracellularly and stimulates superoxide anion generation by direct binding and activation of the NOX2 enzymatic complex.

Conclusions: This study describes a novel molecular mechanism underlying the pro-angiogenic activity of dRP, which involves the sequential activation of NOX2 and NF-κB and the upregulation of VEGFR2.

INTRODUCTION

Angiogenesis is critical for tissue revascularization and repair after injury. ROS have been shown to drive tissue repair by triggering angiogenesis (32). The most important of such factors is VEGF, which is upregulated as a consequence of hypoxia-induced factor-1 (HIF-1) activation (1,28). The increase in ROS triggered by hypoxia and other tissue injuries is associated with oxidation of biological molecules such as lipids and proteins, which has profound effects on cellular physiology (23). Amongst the sources of ROS associated with the stimulation of angiogenesis, NADPH oxidases (or NOXs) have been studied extensively (65,69). The precise links between NOX activation and angiogenesis remain unclear, but several molecular mechanisms have been implicated, including activation of nitric oxide synthase (13) and VEGF upregulation (32,69). Endothelial cells express NOX1, NOX2, NOX4 and NOX5 (18). Amongst NOXs, NOX4 has been shown to lead to stabilization of HIF-1, which in turn stimulates increased transcription of VEGF and drives angiogenesis (69). Other factors, including insulin and TGF-β1, also stimulate angiogenesis in a NOX4-dpendent manner (41,46). Similarly to NOX4, NOX2 is abundantly expressed in endothelial cells and mediates angiogenesis in response to lipopolysaccharide (LPS) and VEGF (19,40). In keeping with their roles as positive regulators of angiogenesis both NOX2 and NOX4 can drive endothelial cell migration and capillary-like tube formation in hyperoxic conditions (45). In addition to their effects on the

HIF/VEGF signaling axis, NOXs have been shown to stimulate angiogenesis through diverse signaling pathways. For example, activation of NF-κB downstream of NOX2 (39) or nuclear factor erythroid 2–related factor 2 (Nrf-2) downstream of NOX4 (57) have been shown to be involved in stimulating the angiogenic responses of endothelial cells.

Deoxyribose-1-phosphate (dRP) has previously been described as an endogenous molecule capable of stimulating angiogenesis in a ROS-dependent manner both *in vitro* and *in vivo* (7,24,42,49,50,58). The generation of dRP in eukaryotic cells is catalyzed by phosphorylases with specificity for different nucleosides. Three main enzymes have been characterized: thymidine phosphorylase (TP), uridine phosphorylased (UP)_and purine nucleoside phosphorylase (PNP) (48). Nucleoside phosphoryalses play a key role in nucleoside and pentose metabolism by degrading nucleosides into free nitrogen base and dRP, with dRP converted to deoxyribose-5-phosphate by phosphopentomutase (64). Several studies have suggested that nucleoside phosphorylases stimulate cancer angiogenesis in solid tumors and participate in the progression of the disease (27,31,62). Although the regulation of nucleoside phosphorylases is largely unknown and their consistutive activity has been described (5), we previously presented data on the release of dRP by human platelets in response to cellular stimulation (67). In this study, we have evaluated the pro-angiogenic activity of dRP on human umbilical vein endothelial cells (HUVECs) *in vitro* using a variety of molecular techniques and have identified a NOX2-NF-κB signaling axis that is engaged by dRP, resulting in the upregulation of VEGFR2 expression and stimulation of angiogenic responses. This study is the most comprehensive and exhaustive characterization of dRP as a pro-angiogenic stimulus to date. Understanding the molecular mechanisms underlying the actions of dRP as a pro-angiogenic stimulus will have important applications in cancer, vascular and regenerative medicine.

RESULTS

dRP stimulates increased levels of ROS generation in a NADPH oxidase-dependent manner

We have previously described the release of dRP by human platelets (67). Using a quantitative LC-MS method, we quantified dRP released by human platelets and mouse macrophages. In platelet suspensions at physiological density (i.e. $3x10^8$/ml) and in culture medium from confluent murine macrophages, dRP reached concentrations above 10μM (Fig. 1A). The ability of dRP to induce the formation of capillary-like structures by endothelial cells *in vitro* (i.e. endothelial 'tubes') was confirmed for concentrations as low as 2μM using low serum and growth factor-reduced Matrigel® (Fig. 1B and Fig. S1A), while other pentoses were not effective (Fig. S2). We also confirmed that dRP concentrations as low as 8μM stimulate a significant increase in endothelial cell ROS formation (while 2μM dRP produced a trend towards increased ROS formation without reaching statistical significance), as measured using dihydroethidium (DHE) after 1 hour of treatment (Fig. 1C). Complete time courses of ROS generation at low micromolar dRP concentrations are shown in supplementary Fig. S1B. The dRP-dependent increase in ROS generation rates was abolished in the presence of 1mM N-acetyl-L-cysteine (NAC), 10μM MnTBAP or 10μM Tempol (Fig. 1D). The link between oxidative stress and angiogenic activity of HUVECs and the role of ROS generation in the angiogenic response induced by dRP were then tested using the ROS scavenger NAC (71) and the SOD mimetics Mn(III)tetrakis(4-benzoic acid)porphyrin (MnTBAP) (21) and 4-hydroxy-2,2,6,6-

tetramethylpiperidin-1-oxyl (Tempol) (33). All three significantly impaired the tubulogenic activity of dRP~~, but not VEGF A~~ (Fig. 1E). Other angiogenic responses induced by dRP (i.e. endothelial cell proliferation and monolayer scratch healing) were also inhibited by NAC, MnTBAP and Tempol (Fig. S3). Interestingly, the stimulatory effect of VEGF on endothelial tube formation (Fig. S4) and monolayer scratch healing (Fig. S5) was abolished by NOX inhibitors (e.g. pan-NOX inhibitor VAS2870 and the NOX2-specific inhibitor peptide Nox2ds-tat) but not ROS scavengers (e.g. NAC) and SOD mimetics (e.g. MnTBAP).

Next, we tested the effect of dRP on redox homeostasis in HUVECs by electron paramagnetic resonance (EPR) using the superoxide-specific spin probe 3-methoxycarbonyl-2,2,5,5-tetramethylpyrrolidine (CMH) (Fig. 2). In these experiments we detected a significant increase in superoxide anion generation rate in response to dRP from 9.7 ± 2.9 to 41.3 ± 4.6 pmol per minute per mg of cell protein (mean ± SEM; shown in Fig. 2A with calibration curve shown in Fig. 2C). Superoxide anion generation detected by EPR was inhibited by the SOD mimetic MnTBAP and by the pan-NOX inhibitor VAS2870 (Fig. 2B). The involvement of NOXs was also confirmed by co-immunoprecipitation of p47phox with NOX2 in the presence of dRP, but not in its absence (Fig. 2D).

dRP directly stimulates NOX2

EPR analysis remains laborious and time consuming, which limits its application for large numbers of samples. Therefore, we also performed ROS generation analysis using live cell imaging with DHE, which confirmed dRP-induced ROS production in HUVECs. We then explored the source(s) of ROS generated in response to dRP. Treatment with the pan-NOX inhibitor VAS2870 (1μM) suppressed the dRP-induced increase in ROS generation (Fig. 3A).

The specific inhibitory peptide Nox2ds-tat (54) was used to show that NOX2 is responsible for the stimulation of ROS generation by dRP. Treatment with Nox2ds-tat completely abolished the dRP-dependent increase in ROS generation in endothelial cells (Fig. 3B). Genetic silencing of NOX2 (i.e.gp91phox subunit) also totally inhibited the dRP-dependent increase in ROS generation rate (Fig. 3C) and endothelial tube formation (Fig. 3D). In contrast, genetic silencing of NOX4 did not significantly impair dRP-dependent ROS generation (Fig. 3E) or endothelial tube formation (Fig. 3F).

In order to test whether dRP acts intracellularly, we treated HUVECs for 30 minutes with 200μM dRP. Following cell disruption by ultracentrifugation, the cytoplasmic fractions were analysed using LC-MS for the presence of dRP. Interestingly, dRP appeared in the cytoplasm of HUVECs after treatment (Fig 4A). As dRP is administered as a salt, the counter ion cyclohexylammonium was utilised as a control and was found only in the culture media, never in the cytoplasmic fractions (data not shown). This suggested the existence of a specific transporter for dRP. Previous studies indicated that the transporter, GLUT1, is the endothelial transporter for several monosaccharides besides hexoses, including riboses (60). To test the hypothesis that GLUT1 is responsible for the internalisation of dRP, we utilised two specific inhibitors of this transporter: fasentin and STF-31 (10μM). These inhibitors abolished the ability of dRP to stimulate endothelial tube formation on Matrigel® , without affecting VEGF-stimulated tube formation (Fig. 4B). GLUT1 was then silenced by siRNA which resulted in a significant inhibition of dRP-dependent ROS generation (Fig. 4C) and tube formation (Fig. 4D). These data suggest that GLUT1 plays a significant role in the internalisation and pro-angiogenic activity of dRP. VEGF-dependent tube formation was not affected by depletion of GLUT1 (Fig. 4D).

Direct binding of dRP to the NOX2 complex (but not to NOX4 or NOX1) was then demonstrated by pull-down experiments using biotinylated dRP and streptavidin beads. In these experiments, dRP was conjugated with biotin in a reaction leading to a mixture of 3 different adducts (C3-O-linked, C5-O-linked and C1-OP-linked; Fig 5A). NOX2 (but not NOX4 or NOX1) was selectively pulled down in the presence of biotinylated dRP, but not in the presence of non-biotinylated dRP. The ability of dRP to activate NOXs directly without the mediation of intracellular signaling pathways was then investigated using a cell-free superoxide anion generation assay (9). Following cell fractionation, HUVEC cytosolic and membrane fractions were characterized for the expression of NOX1, NOX2 and NOX4. All three NOXs are expressed in the membrane fraction but not in the cytoplasmic fraction (Fig. 5B). Caveolin-1 and actin were used as membrane and cytoplasmic markers, respectively. Upon treatment with dRP, HUVEC membrane fractions induced a significant increase in ferrous cytochrome c compared to membrane fractions treated with vehicle alone. The formation of ferrous cytochrome c was inhibited in the presence of SOD and by the non-specific flavoenzyme inhibitor DPI. The dRP-dependent response registered in this assay was also inhibited by the highly specific peptide inhibitor Nox2ds-tat (54), which has been used for membrane-based cell-free assays previously (14) Taken together, these data suggest that dRP is able to directly activate NOX2 without the mediation of other signaling events.

In order to confirm the oxidative status induced by dRP, biotinyl-iodoacetamide (BIAM) and HRP-streptavidin were utilized to stain free thiols in HUVEC proteins. These experiments demonstrated that a 4 hour exposure to 200μM dRP induces cysteine oxidation (i.e. formation of sulfenic acid and/or disulfide bonds), which appears as a loss BIAM staining (Fig. 6A). Several bands disappear or become significantly fainter upon treatment with dRP (green arrows in Fig.

6A), which suggests that this molecule induces pro-oxidative cell conditions, leading to oxidation of cysteines in several proteins (as expected from the activation of a highly expressed pro-oxidative enzyme such as NOX2). Protein thiol oxidation (Fig. 6B) without induction of cell apoptosis (Fig. 6C), was confirmed by free thiol staining and annexin V binding, respectively.

dRP induces activation of NF-κB in a NOX-dependent manner

Several redox-dependent transcription factors, including HIF-1 (51), Nrf2 (30,34) and NF-κB (11,56), play an important role in endothelial cell responses. To probe the involvement of HIF-1, Nrf2 and NF-κB as mediators of the pro-angiogenic activities of dRP, we tested the DNA binding activity of these transcription factors in HUVECs treated with dRP (53). These experiments revealed that NF-κB is strongly activated in the presence of dRP (Fig. 7A), whereas HIF-1 and Nrf-2 did not show any significant activation (Fig. S~~3~~6B). In agreement with these results, dRP increased p65-NF-κB levels in the nuclear fraction of HUVECs (as a result of nuclear translocation; Fig. 7B) and promoted NF-κB phosphorylation on Ser468 (but not Ser536; Fig. 7C and Fig. S~~3~~6A). Translocation of NF-κB to the nucleus upon dRP treatment was confirmed by immunolabelling and confocal imaging (Fig. 7D). Treatment with the non-specific flavoenzyme inhibitor DPI or direct inhibition of NF-κB with the potent inhibitor N4-[2-(4-phenoxyphenyl)ethyl]-4,6-quinazolinediamine (QNZ) (61) abolished nuclear translocation of NF-κB. In common with DPI, NOX2 inhibition by the peptide Nox2ds-tat and genetic silencing of p22phox or NOX2 abolished translocation of NF-κB to the nucleus in dRP-stimulated HUVECs (Fig. 8A). Collectively, these data suggest that dRP-dependent activation of NOX2 is responsible for NF-κB activation. The functional role of NF-κB in the pro-angiogenic activity of dRP was tested by siRNA-dependent genetic silencing of this transcription factor (Fig. 8B), which resulted in complete inhibition of endothelial tube formation in response to dRP.

dRP-dependent activation of NF-κB upregulates VEGFR2 and induces endothelial tube formation

An initial analysis of the expression of angiogenic factors in HUVECs by ELISA (Fig. S74A) and immunoblotting (Fig. S476B) did not detect any significant change in response to dRP, suggesting that the effects of dRP do not depend upon autocrine production of these factors. Further studies, however, showed that VEGFR2 is robustly upregulated at the mRNA and protein levels in HUVECs following exposure to dRP (Fig. 9A-D). The NF-κB inhibitor QNZ ablated the expression of VEGFR2 in HUVECs and inhibited the upregulation of this receptor by dRP, suggesting a critical role for NF-κB in the expression of VEGFR2 (Fig. 9C). The NOX2 inhibitor Nox2ds-tat (54) significantly reduced upregulation of VEGFR2 by dRP (Fig 9D). The functional relevance of VEGFR2 upregulation for the pro-angiogenic activity of dRP was confirmed in experiments using the VEGFR2 inhibitor Pazopanib and the VEGFR2-specific inhibitory antibody MAB3572, both of which abolished tubulogenesis stimulated by dRP (Fig. 9E). Experiments with the NF-κB inhibitor QNZ suggested that this transcription factor is necessary for dRP-dependent tube formation (Fig. 9F), which correlates with the strong effect of NF-κB inhibition on VEGFR2 expression shown in Fig. 9B, and the involvement of VEGFR2 in dRP-dependent angiogenesis shown in Fig. 9E.

dRP stimulates VEGFR2 upregulation and NOX2-dependent angiogenesis *in vivo*

The pro-angiogenic activity of dRP has been described previously (35,38,49,50). In order to confirm that the mechanism of action of dRP that we characterized *in vitro* also occurs *in vivo*, we applied dRP to excisional wounds in mice and assessed the levels of tissue vascularisation by hematoxylin staining (Figure 10A) and VEGFR2 expressedion at the wound site 7 days after application (Figure 10B). These experiments showed a significant increase in both wound

vascularity and ~~the~~ expression of VEGFR2 in wounds treated with dRP ~~(Fig. 10A)~~. The dependence of dRP pro-angiogenic activity on NOX2 was then tested in NOX2$^{-/-}$ mice. Using a Matrigel™ plug vascularisation assay, we demonstrated that the presence of dRP stimulated a significantly higher vascularisation of the plug in wild type animals compared to NOX2$^{-/-}$ mice. This was ~~(as~~ demonstrated by hematoxylin (Figure 10C) and endothelial-specific CD31 staining (Figure 10D)~~, while in NOX2$^{-/-}$ mice the dRP-dependent vascularisation was absent (Fig. 10B).~~

DISCUSSION

The pro-angiogenic activity of dRP has been described previously, although the mechanism of action has remained elusive. The dRP-generating enzyme thymidine phosphorylase (TP) was initially cloned as platelet-derived endothelial cell growth factor (PD-ECGF) and characterized for its proangiogenic properties (27). Local injection of TP or TP-expressing cells has been shown to induce tissue neovascularization *in vivo*, which depends on the enzymatic activity of TP and the generation of dRP (35). TP and other dRP-generating enzymes such as purine nucleoside phosphorylase (PNP) and uridine phosphorylase (UP), are overexpressed in cancers and associated with cancer vascularisation and metastasis (31). In our studies, we identified platelets and macrophages as key generators of micromolar concentrations of dRP (49), whereas endothelial cells do not synthesise detectable levels of dRP and recognise this molecule (or its dephosphorylation product 2-deoxy-D-ribose) as a paracrine signal that triggers angiogenesis (6).

Here, we demonstrate for the first time that the oxidative response induced by dRP in endothelial cells is mediated by NOX2, and that dRP can directly bind and activate this enzyme. Importantly, we showed that dRP binds and pulls down NOX2 but not NOX1 or NOX4 from

endothelial cell lysates. As NOX1 and NOX2 complexes share several regulatory subunits (i.e. p22phox, p47phox and Rac1), the specific pull-down of NOX2 and not NOX1 by biotinylated dRP supports the hypothesis that dRP directly interacts with the NOX2 enzymatic subunit (also known as gp91phox). Direct binding and activation of a NOX complex is a remarkable and rarely reported mode of action for a signalling molecule, which has been described in only a few recent studies. Arachidonic acid has been shown to activate NOX2 by promoting its interaction with the p67phox/Rac1 complex (37). In this case, the authors proposed that arachidonic acid interacts directly with p67phox. The involvement of p47phox, p67phox or other subunits in the dRP-dependent activation of NOX2 demonstrated in our study cannot be excluded at present, but the initial binding appears to be to NOX2.

A correlation between NOX-dependent ROS generation and angiogenesis has been described previously. NOX4 and NOX2 both play prominent roles in the stimulation of angiogenic responses of endothelial cells (15,39,40,63,69), whereas NOX1 and NOX5 have received less attention (3,4). In particular, a link between NOX2 and NOX4 activity and increased endothelial cell motility has been reported (26,45). In our study, NOX2 activation by dRP leads to NF-κB activation (as shown by several approaches including p65-NFkB translocation and phosphorylation), which appears critical in the pro-angiogenic signaling cascade triggered by dRP. The role of of NF-kB in the signaling cascade stimulated by dRP was demonstrated using both the QNZ inhibitor (which has low nanomolar potency on NF-kB but can also inhibit store-operated calcium channels at hich nanomolar concentrations (68)) and genetic silencing of p65-NF-κB. This is in agreement with recent studies showing activation of NF-κB downstream of NOX2 in angiogenic responses of endothelial cells (40). However, in contrast to this latter study,

we did not detect any significant changes in the expression of VEGF-A or angiopoietin-2 in response to dRP treatment. One possible explanation for these contrasting findings is the source of the endothelial cells used in the two studies (i.e. human umbilical vein *versus* human pulmonary microvasculature). Instead, we identified VEGFR2 as a key component of the NF-κB-mediated angiogenic response stimulated by dRP. This is in keeping with previous studies showing that the promoter of VEGFR2 contains NF-kB-binding motives (55) and recent studies showing regulation of VEGFR2 expression by NF-κB (17). Importantly, we confirmed VEGFR2 upregulation by dRP *in vivo* using a mouse excisional wound assay.

Several previous studies have highlighted associations between endothelial cell oxidative status and the angiogenic response. For example, the link between ROS formation in hypoxic conditions and the activity of HIF-1 has been described (22). Although additional routes have also been proposed (2), ROS have been shown to promote HIF-1-dependent transcription via inactivation of prolyl hydroxylase and reduction of HIF proteasome-dependent degradation (47). The activation of NOX4 and NOX3, but not NOX2, has previously been associated with HIF-1 activation (8,69), whereas NOX2 has been shown to stimulate NF-κB activation in endothelial cells (40). Since we have identified NOX2 as a key target of dRP biological activity, our data support the existing literature showing that NF-κB, as opposed to HIF-1, is activated by this member of the NOX family. We confirmed that NOX2 is also necessary for the pro-angiogenic effect of dRP *in vivo*. This is in line with two recent studies showing a role for this member of the NADPH oxidase family in the stimulation of angiogenesis *in vivo*, although it should be emphasized that these reports, in contrast to the present study, did not provide clarity on the underlying molecular mechanisms (10,70).

Interestingly, we observed direct cysteine oxidation in endothelial cells treated with dRP (as demonstrated by the loss of free thiols). The product of cysteine oxidation by ROS in mammalian cells is cysteine sulfenic acid, which can undergo further oxidation to generate cysteine sulfinic acid and cysteine sulfonic acid, or can form intramolecular or intermolecular disulfide bridges (16). The oxidation of cysteine by ROS has important functional consequences for protein phosphatases and protein kinases (52). For example, and relevant to our study, ROS-induced serine and/or tyrosine phosphorylation, ubiquitination and consequent proteolytic degradation of the inhibitor subunit IκB are responsible for nuclear transportation and activation of NF-κB (43). These observations support our data showing ROS-dependent activation of NF-κB in response to dRP.

Overall, this study has comprehensively elucidated the mechanism of action of dRP, a small molecule with pro-angiogenic effects *in vitro* and *in vivo* (49). We showed that, similarly to other sugars (either hexoses or pentoses) (29,44), dRP is readily internalised by endothelial cells and that the transporter GLUT1 is the most likely transporter responsible fo this. This is in agreement with previous studies suggesting that TP stimulates endothelial cells in a "non-receptor-mediated" manner (6). Once internalized, dRP has the remarkable ability to directly bind and activate NOX2, but not NOX4 or NOX1. Activation of NOX2 and the resulting generation of ROS trigger NF-κB activation and promote angiogenic responses in endothelial cells, which depend on the activity of VEGFR2. This study, therefore, represents a milestone in the understanding of the pro-angiogenic activity of the dRP-generating enzyme thymidine

phosphorylase, which was cloned as platelet-derived endothelial growth factor and characterized as a potent stimulator of angiogenesis in the late 1980s (27).

INNOVATION

A novel paracrine signaling pathway is described in this study, whereby the angiogenic stimulus 2-deoxyribose-1-phosphate (dRP) released by platelets, macrophages and cancer cells is internalised by endothelial cells and acts intracellularly by directly activating NADPH oxidase 2 (NOX2). In turn, this leads to nuclear factor kappa B (NF-κB)-dependent upregulation of VEGF receptor 2 (VEGFR2) and VEGF-dependent angiogenesis. Our elucidation of the mechanism of action of dRP is critical for understanding the full potential of this pro-angiogenic paracrine signal, which may find important applications in regenerative, vascular and cancer medicine.

MATERIALS AND METHODS

LC-MS detection and quantification of dRP. Macrophages were differentiated from whole bone marrow cultures from B57BL6 mice in Dulbecco's modified Eagle's medium (DMEM) + 10% L929 cell conditioned medium, 10% fetal bovine serum and 1X penicillin/streptomycin. Activation of macrophages was performed with 100 ng/mL lipopolysaccharide (LPS) and 100 ng/mL interferon gamma (IFNγ) or 20 ng/mL interleukin 4 (IL4) and 50 ng/mL IFNγ. Platelets were isolated via two-step centrifugation, as previously described (66). Activation was obtained with 0.1 unit/ml thrombin or 10 µg/ml collagen for 10 minutes in an aggregometer at 700 rpm. Endothelial cells with or without dRP incubation (200µM), where washed with PBS three times and lysed by ultrasonication. For all samples (i.e. cell extracts obtained by ultrasonication or culture supernatants), proteins were eliminated by acetonitrile precipitation. QTOF-UHPLC analysis was conducted using a MaXis HD quadrupole electrospray time-of-flight (ESI-QTOF) mass spectrometer (Bruker Daltonik GmbH, Bremen, Germany), which was coupled to an Ultimate 3000 UHPLC (Thermo Fisher Scientific, California, USA). Liquid chromatography was performed using a Dionex Acclaim RSLC PolarAdvantage II (PA2), 2.2 µM, 120Å, 2.1 x 50 mm reverse phase column (Thermo Fisher Scientific, California, USA) with a flow rate of 0.4

mL/min, and an injection volume of 10 µL. Mobile phases A and B consisted of 1mM ammonium fluoride in water, and methanol, respectively. Deoxyribose-1-phosphate was detected as [M-H]- ion with a mass-to-charge (m/z) ratio of 314.0120 ± 0.005 Da.

Endothelial cell culture

HUVECs were isolated from umbilical veins as described previously (25). HUVECs were cultured and passaged in medium M199 supplemented with 20% FBS, 4 mM glutamine, 100 units/mL penicillin, 100 units/mL streptomycin and 20 mM $NaHCO_3$ and cultured in flasks pre-coated with 1% gelatin (w/v).

***In vitro* capillary-like tube formation assay**

Growth factor reduced (GFR) Matrigel® was utilized to provide extracellular matrix for cell culture. 10^4~~,000~~ cells/well in 100µl of M199 (no FBS) were added to 96-well microplates containing 65µl GFR Matrigel® per well. Phase contrast images were captured 4 hours after treatment using an EVOS FL microscope with a 4x /0.1 Plan-Achromat objective. Total number of tubes was measured using the Angiogenesis Analyzer plugin of ImageJ.

Formatted: Superscript

Intracellular live-cell ROS generation assay

HUVECs were plated into 96-well black, optically clear bottom tissue culture sterile plates and were cultured for 24 h to reach ~70% confluence. Cells were washed once with PBS, pre-treated with inhibitors for 30 minutes (as indicated in the figure legends) and then treated with 5µM DHE and dRP at the desired concentrations. Fluorescence was monitored using a CLARIOstar®

plate reader at 37°C with atmospheric control at 5% CO_2/20% O_2. Fluorescence was measured at Ex/Em: 510/610nm over 2 hours.

Superoxide detection using EPR

HUVECs cultured in 6-well plates were washed twice with EPR-Krebs HEPES buffer (EPR-KHB) adjusted to pH 7.4 and then incubated for 1 hour in deoxygenated EPR-KHB (+1 g/l glucose) in the presence of treatments. Cell-permeable superoxide-specific spin probe 3-methoxycarbonyl-2,2,5,5-tetramethylpyrrolidine (CMH) at a final concentration of 200μM (from 10mM CMH stock solution in the presence of 25uM deferoxamine and 5uM DETC) was then added for 45 minutes. The supernatant was then analysed using a Bruker e-scan with the following settings: center field 1.99g, microwave power 20mW, modulation amplitude 2G, sweep time 10s, number of scans 10 and field sweep 60G. Calibration curve was calculated using kwnon concentrations of CM• (CM-radical, purchased from Noxygen #NOX-18.2), as shown in Fig. 2C. Data are presented as pmols of superoxide anion divided by incubation time in minutes and amount of protein per well in mg, calculated using the bicinchoninic assay method.

Determination of NADPH oxidase activity in endothelial membranes

The membrane fraction of HUVECs was separated by ultrasonication and ultracentrifugation (100,000 g for 60 minutes). NADPH oxidase activity in the membrane fraction was measured as previously described (9). Superoxide production was measured in PBS (140 mM NaCl, 2.7 mM KCl, 10 mM Na_2HPO_4, 2 mM KH_2PO_4, pH 7.4) containing 100μg of the membrane fraction, 10mM diethyldithiocarbamate, 100μM NADPH, 80μM acetylated cytochrome C, 1000 U/mL

catalase, and 100μM EDTA. 10μM diphenylene iodonium (DPI) and 1000 U/mL SOD were used to inhibit and scavenge ROS, respectively.

ELISA-based assay for transcription factor activation

DNA-binding capacity of NF-κB was determined in whole extracts of HUVECs treated as indicated using the TransAM® method according to the suppliers' instructions.

Immunofluorescence of NF-κB translocation

HUVECs were grown on coverslips to 60–70% confluence and treated with stimuli/inhibitors. Following fixation in 4% w/v paraformaldehyde, cells were stained with anti-p65-NF-κB (1:50), Alexa Fluor® 488 Rabbit Anti-Mouse (1:200) and 4′,6-diamidino-2-phenylindole (DAPI, 1:100). Slides were examined using the 60× 1.40 NA oil objective on a LSM 510 META confocal microscope (Carl Zeiss AG, Jena, Germany).

Real-Time Quantitative PCR (qPCR)

qPCR was performed on a ViiA7 Real-Time PCR System using Power SYBR Green PCR and 300 nM gene-specific primers (VEGFR2: 5′CCAGTGTCATTTCCGATCACT TT and 5′-GGCCCAATAATCAGAGTGGCA and GAPDH: 5′-AGCCGCATCTTCTTT TGCGT and 5′-TGACGAACATGGGGGCATCA). The amplification of a single PCR product was confirmed by melting curve analysis. Gene-specific mRNA levels were estimated by the $2^{-\Delta\Delta Ct}$ analysis and normalized against GAPDH levels to obtain relative changes in gene expression.

Immunoprecipitation and immunoblotting

For immunoprecipitation, HUVECs cultured in 6 well-microplates were lysed in 500 µL of ice-cold lysis buffer (50 mM Tris-HCl, pH 8.0, 150 mM NaCl, and 0.1% Triton X-100 containing protease and phosphatase inhibitors). The suspension was ultrasonicated using a 150VT Ultrasonic Homogenizer (BioLogics, Manassas, VA, USA). Primary antibody and protein A/G Plus-Agarose were used for immunoprecipitation. Immunoprecipitates were subjected to SDS−polyacrylamide gel electrophoresis (SDS-PAGE) and transferred to polyvinylidene difluoride (PVDF) for immunoblotting. For immunoblotting cells were lysed in RIPA buffer (1% v/v Triton X-100, 1% w/v sodium deoxycholate, 0.1% w/v SDS, 150 mM NaCl, 5 mM EDTA, 50 mM Tris pH 7.4).

siRNA-mediated gene silencing

HUVECs were transfected with NOX2 (sc-35503), NOX4 (sc-41586), p65 NF-κB (sc-29410), p22phox (sc-36149) or scrambled control (sc-37007) siRNAs (Santa Cruz Biotechnology). The siRNAs were diluted to 100nM in transfection medium (sc-36868; Santa Cruz Biotechnology) containing transfection reagent (sc-29528; Santa Cruz Biotechnology), incubated for 45 min at room temperature and then further diluted to 20nM in transfection medium. The cells were covered with this solution and incubated for 3 h at 37 °C. The solution was then replaced with fresh culture medium and cells used for experiments 72 hours after transfection.

Preparation of a biotinylated dRP bait and streptavidin pull-down assay

0.6mg/ml dRP was resuspended in anhydrous DMSO and 1,1′-carbonyldiimidazole. The resulting solution was stirred for 24 h. In a separate vessel, N-(+)-biotinyl-3-aminopropylammonium trifluoroacetate was taken up in anhydrous dimethylformamide and

N,N-diisopropylethylamine added. After 30 minutes, the solvents were evaporated to dryness and the DMSO solution of activated dRP was added. The resulting solution was stirred for 72 h before being divided into 10 equal portions and the solvents removed under vacuum. HUVECs were scraped on ice into 10mM Tris plus 0.3M sucrose buffer (pH 7.1). The suspension was sonicated on ice and centrifuged at 1,000g for 5 minutes. The lysate were treated with biotinylated-dRP or biotin as control for 1 hour under rotation at 4 °C. Streptavidin beads were added to samples, which were further rotated for 2 hours at 4 °C. Samples were boiled, loaded on to SDS-PAGE gels and resulting blots probed for NOX 1, 2 and 4, and for β-actin as loading control.

Intracellular free-thiol monitoring by cysteine labeling

Biotinyl-iodoacetamide (BIAM) was used to label free thiols in cell lysates as previously described (12). Cell lysates were obtained by sonication in anoxic conditions (cell lysis buffer: 150 mM NaCl, 0.5% v/v Triton-X, 50 mM Tris-HCl, pH 6.5, Complete™ protease inhibitors). Cell lysates were labeled for 2 hours with 20μM BIAM in anoxic conditions. BIAM was then quenched with 10 mM β-mercaptoethanol. Cell proteins were separated by SDS-PAGE, stained with Streptavidin-HRP and visualized by enhanced chemiluminescence.

Alternatively, VitaBright-43™ was used to label free thiol groups on proteins (59). This reagent is cell permeable and gives thioester-coupled fluorescent products in a quantitative manner, which allows an estimate of cell oxidative state. $5x10^6$ cells/ml treated as described were labeled with VitaBright-43™ and propidium iodide as suggested by suppliers. NucleoCounter3000 (Chemometec A/S) was utilized to analyse cell fluorescence levels associated to the two dyes.

Flow cytometry analysis of apoptosis

Staining with annexin V-FITC to detect cell surface exposure of phosphatidylserine was performed to examine apoptosis in cultured HUVEC treated with or without dRP for 24 hours (50). During apoptosis, an early and ubiquitous event is the exposure of phosphatidylserine at the cell surface, which is detected with annexin V-FITC. Cells treated with 5mM diethyl maleate for 24 hours served as a pro-apoptopic control. After incubation, cells were harvested with the gentle dissociating buffer TrypLE®, pelleted by centrifugation, washed with PBS, and resuspended in PBS. Cell suspensions were stained with Annexin V/FITC according to the manufacturer's instructions. Briefly, PBS-washed cells were suspended in 100 µl FITC binding buffer at a minimum concentration of 1×10^6 combined with 5 µl Annexin V/FITC. After 15 minutes of incubation in the dark on ice, cells were centrifuged at 2000 rpm for 10 minutes, resuspended in PBS, and analysed using a FACSCanto II (BD Biosciences). Cells that were annexin V-negative were considered viable cells. Cells positive for annexin V were considered apoptotic. All samples were prepared in triplicate.

Mouse wound healing

Mouse maintainance and experimental procedures were performed according to local ethic approval and a dedicated UK Home Office Project licence. Wounding was performed as described by Mahdipour and Mace (2012) (36). dRP pellets were produced by diluting dRP into PBS:methyl cellulose (1%) (1:1). 50 µl of this solution was then spotted and dried to form a pellet containing 10.3µg (25nmol) of dRP. Control pellets were generated in the same way by adding vehicle solution (PBS) instead of dRP. Pellets were administered immediately following wounding and rehydrated directly into the wound. Pellets were subsequently administered every other day on days 2, 4 and 6. Wounds were harvested at day 7, as appropriate, from sacrificed

animals with a 2mm border, fixed in formalin and embedded in paraffin. Tissues were sectioned using a Leica CM3050 S to produce serial sections of 10µm thickness. Following de-waxing in xylene/EtOH/MetOH, sections were stained with anti-VEGFR2/KDR/Flk-1 antibodies (1:100, R&D Systems #AF644) and FITC-labelled anti-goat IgG secondary antibodies (1:200, Life Technologies). Images were captured using a EVOS FL microscope with a 4x /0.1 Plan-Achromat objective (red fluorescence channel and phase contrast). Alternatively, tissue sections were cut at 5µm thickness and stained with hematoxylin/eosin using the Mayer's method (20). Sections were evaluated for vascularity by imaging using a Olympus CKX41 microscope with UPlanFl 4x/0.13 objective.

Matrigel plug vascularization assay

Mouse maintainance and experimental procedures were performed according to local ethic approval and a dedicated UK Home Office Project licence. Wild type (C57BL6/J) and NOX2$^{-/-}$ (Jackson Laboratories B6.129S-Cybbtm1Din/J) mice were injected with 200µl of Growth Factor-Redice Matrigel™ (Corning) containing 41.2µg (100nmol) of dRP or an equivalent volume of vehicle solution (PBS). 7 days after injection, the animals were euthanised and the matrigel plug was explanted, fixed in 10% formalin and embedded in paraffin. Tissues were sectioned using a Leica CM3050 S to produce serial sections of 50µm thickness. Following de-waxing in xylene/EtOH/MetOH, sections were either stained with hematoxylin or anti-CD31 antibodies (1:100, Cell Signaling Technologies #3528), TRITC-labelled anti-mouse IgG secondary antibodies (1:200, Life Technologies) and 0.25µg/ml DAPI (4′,6-diamidino-2-phenylindole). Images were captured using a EVOS FL microscope with a 4x /0.1 Plan-Achromat objective (red and blue fluorescence channels and phase contrast). Alternatively,

tissue sections were cut at 5µm thickness and stained with hematoxylin using the Mayer's method (20). Sections were evaluated for vascularity by imaging using a Olympus CKX41 microscope with UPlanFl 4x/0.13 objective.

ACNOWLEDGEMENTS

This work was sponsored by the Biotechnology and Biological Sciences Research Council (BB/J002690/1), the Medical Research Council (MRC/CIC/2015) and the British Heart Foundation (PG/15/40/31522). We acknowledge Dr Adrian Rogers for help with imaging and flow cytometry. DV and GP designed, performed and analysed experiments. JMS performed chemistry experiments to conjugate dRP to agarose beads. TMF performed qPCR experiments. HM provided expertise and logistics for HUVEC isolation. MB and KM performed experiments for the quantification of dRP in macrophages. SR and AL performed LC-MS for dRP quantification. CW-J was involved in the initial conception of the study, provided expertise for HUVEC isolation and assessment of angiogenesis in vitro, and commented on the manuscript. GP wrote the manuscript.

AUTHOR DISCLOSURE STATEMENT

No competing financial interest is declared.

REFERENCES

1. Ahluwalia A, Tarnawski AS. Critical role of hypoxia sensor--HIF-1alpha in VEGF gene activation. Implications for angiogenesis and tissue injury healing. *Curr Med Chem* 19: 90-7, 2012.
2. Alig SK, Stampnik Y, Pircher J, Rotter R, Gaitzsch E, Ribeiro A, Wornle M, Krotz F, Mannell H. The tyrosine phosphatase SHP-1 regulates hypoxia inducible factor-1alpha (HIF-1alpha) protein levels in endothelial cells under hypoxia. *PLoS One* 10: e0121113, 2015.
3. Arbiser JL, Petros J, Klafter R, Govindajaran B, McLaughlin ER, Brown LF, Cohen C, Moses M, Kilroy S, Arnold RS, Lambeth JD. Reactive oxygen generated by Nox1 triggers the angiogenic switch. *Proc Natl Acad Sci U S A* 99: 715-20, 2002.
4. BelAiba RS, Djordjevic T, Petry A, Diemer K, Bonello S, Banfi B, Hess J, Pogrebniak A, Bickel C, Gorlach A. NOX5 variants are functionally active in endothelial cells. *Free Radic Biol Med* 42: 446-59, 2007.
5. Bijnsdorp IV, Azijli K, Jansen EE, Wamelink MM, Jakobs C, Struys EA, Fukushima M, Kruyt FA, Peters GJ. Accumulation of thymidine-derived sugars in thymidine phosphorylase overexpressing cells. *Biochem Pharmacol* 80: 786-92, 2010.
6. Brown NS, Bicknell R. Thymidine phosphorylase, 2-deoxy-D-ribose and angiogenesis. *Biochem J* 334 (Pt 1): 1-8, 1998.
7. Brown NS, Jones A, Fujiyama C, Harris AL, Bicknell R. Thymidine phosphorylase induces carcinoma cell oxidative stress and promotes secretion of angiogenic factors. *Cancer Res* 60: 6298-302, 2000.
8. Carnesecchi S, Carpentier JL, Foti M, Szanto I. Insulin-induced vascular endothelial growth factor expression is mediated by the NADPH oxidase NOX3. *Exp Cell Res* 312: 3413-24, 2006.
9. Cayatte AJ, Rupin A, Oliver-Krasinski J, Maitland K, Sansilvestri-Morel P, Boussard MF, Wierzbicki M, Verbeuren TJ, Cohen RA. S17834, a new inhibitor of cell adhesion and atherosclerosis that targets nadph oxidase. *Arterioscler Thromb Vasc Biol* 21: 1577-84, 2001.

10. Chan EC, van Wijngaarden P, Chan E, Ngo D, Wang JH, Peshavariya HM, Dusting GJ, Liu GS. NADPH oxidase 2 plays a role in experimental corneal neovascularization. *Clin Sci (Lond)* 130: 683-96, 2016.
11. Chandel NS, Trzyna WC, McClintock DS, Schumacker PT. Role of oxidants in NF-kappa B activation and TNF-alpha gene transcription induced by hypoxia and endotoxin. *J Immunol* 165: 1013-21, 2000.
12. Choi KS, Park SY, Baek SH, Dey-Rao R, Park YM, Zhang H, Ip C, Park EM, Kim YH, Park JH. Analysis of protein redox modification by hypoxia. *Prep Biochem Biotechnol* 36: 65-79, 2006.
13. Craige SM, Chen K, Pei Y, Li C, Huang X, Chen C, Shibata R, Sato K, Walsh K, Keaney JF, Jr. NADPH oxidase 4 promotes endothelial angiogenesis through endothelial nitric oxide synthase activation. *Circulation* 124: 731-40, 2011.
14. Csanyi G, Cifuentes-Pagano E, Al Ghouleh I, Ranayhossaini DJ, Egana L, Lopes LR, Jackson HM, Kelley EE, Pagano PJ. Nox2 B-loop peptide, Nox2ds, specifically inhibits the NADPH oxidase Nox2. *Free Radic Biol Med* 51: 1116-25, 2011.
15. Datla SR, Peshavariya H, Dusting GJ, Mahadev K, Goldstein BJ, Jiang F. Important role of Nox4 type NADPH oxidase in angiogenic responses in human microvascular endothelial cells in vitro. *Arterioscler Thromb Vasc Biol* 27: 2319-24, 2007.
16. Dickinson BC, Chang CJ. Chemistry and biology of reactive oxygen species in signaling or stress responses. *Nat Chem Biol* 7: 504-11, 2011.
17. Dong F, Zhou X, Li C, Yan S, Deng X, Cao Z, Li L, Tang B, Allen TD, Liu J. Dihydroartemisinin targets VEGFR2 via the NF-kappaB pathway in endothelial cells to inhibit angiogenesis. *Cancer Biol Ther* 15: 1479-88, 2014.
18. Drummond GR, Selemidis S, Griendling KK, Sobey CG. Combating oxidative stress in vascular disease: NADPH oxidases as therapeutic targets. *Nat Rev Drug Discov* 10: 453-71, 2011.
19. Evangelista AM, Thompson MD, Bolotina VM, Tong X, Cohen RA. Nox4- and Nox2-dependent oxidant production is required for VEGF-induced SERCA cysteine-674 S-glutathiolation and endothelial cell migration. *Free Radic Biol Med* 53: 2327-34, 2012.
20. Fischer AH, Jacobson KA, Rose J, Zeller R. Hematoxylin and eosin staining of tissue and cell sections. *CSH Protoc* 2008: pdb prot4986, 2008.
21. Gauuan PJ, Trova MP, Gregor-Boros L, Bocckino SB, Crapo JD, Day BJ. Superoxide dismutase mimetics: synthesis and structure-activity relationship study of MnTBAP analogues. *Bioorg Med Chem* 10: 3013-21, 2002.
22. Guzy RD, Hoyos B, Robin E, Chen H, Liu L, Mansfield KD, Simon MC, Hammerling U, Schumacker PT. Mitochondrial complex III is required for hypoxia-induced ROS production and cellular oxygen sensing. *Cell Metab* 1: 401-8, 2005.
23. Hensley K, Robinson KA, Gabbita SP, Salsman S, Floyd RA. Reactive oxygen species, cell signaling, and cell injury. *Free Radic Biol Med* 28: 1456-62, 2000.
24. Hotchkiss KA, Ashton AW, Klein RS, Lenzi ML, Zhu GH, Schwartz EL. Mechanisms by which tumor cells and monocytes expressing the angiogenic factor thymidine phosphorylase mediate human endothelial cell migration. *Cancer Res* 63: 527-33, 2003.
25. Houliston RA, Pearson JD, Wheeler-Jones CP. Agonist-specific cross talk between ERKs and p38(mapk) regulates PGI(2) synthesis in endothelium. *Am J Physiol Cell Physiol* 281: C1266-76, 2001.

26. Ikeda S, Yamaoka-Tojo M, Hilenski L, Patrushev NA, Anwar GM, Quinn MT, Ushio-Fukai M. IQGAP1 regulates reactive oxygen species-dependent endothelial cell migration through interacting with Nox2. *Arterioscler Thromb Vasc Biol* 25: 2295-300, 2005.
27. Ishikawa F, Miyazono K, Hellman U, Drexler H, Wernstedt C, Hagiwara K, Usuki K, Takaku F, Risau W, Heldin CH. Identification of angiogenic activity and the cloning and expression of platelet-derived endothelial cell growth factor. *Nature* 338: 557-62, 1989.
28. Jiang BH, Semenza GL, Bauer C, Marti HH. Hypoxia-inducible factor 1 levels vary exponentially over a physiologically relevant range of O2 tension. *Am J Physiol* 271: C1172-80, 1996.
29. Kaiser N, Sasson S, Feener EP, Boukobza-Vardi N, Higashi S, Moller DE, Davidheiser S, Przybylski RJ, King GL. Differential regulation of glucose transport and transporters by glucose in vascular endothelial and smooth muscle cells. *Diabetes* 42: 80-9, 1993.
30. Kang KW, Lee SJ, Kim SG. Molecular mechanism of nrf2 activation by oxidative stress. *Antioxid Redox Signal* 7: 1664-73, 2005.
31. Kawahara A, Hattori S, Akiba J, Nakashima K, Taira T, Watari K, Hosoi F, Uba M, Basaki Y, Koufuji K, Shirouzu K, Akiyama S, Kuwano M, Kage M, Ono M. Infiltration of thymidine phosphorylase-positive macrophages is closely associated with tumor angiogenesis and survival in intestinal type gastric cancer. *Oncol Rep* 24: 405-15, 2010.
32. Khatri JJ, Johnson C, Magid R, Lessner SM, Laude KM, Dikalov SI, Harrison DG, Sung HJ, Rong Y, Galis ZS. Vascular oxidant stress enhances progression and angiogenesis of experimental atheroma. *Circulation* 109: 520-5, 2004.
33. Krishna MC, Samuni A, Taira J, Goldstein S, Mitchell JB, Russo A. Stimulation by nitroxides of catalase-like activity of hemeproteins. Kinetics and mechanism. *J Biol Chem* 271: 26018-25, 1996.
34. Latham Birt SH, Purcell R, Botham KM, Wheeler-Jones CP. Endothelial HO-1 induction by model TG-rich lipoproteins is regulated through a NOX4-Nrf2 pathway. *J Lipid Res*, 2016.
35. Liekens S, Hernandez AI, Ribatti D, De Clercq E, Camarasa MJ, Perez-Perez MJ, Balzarini J. The nucleoside derivative 5'-O-trityl-inosine (KIN59) suppresses thymidine phosphorylase-triggered angiogenesis via a noncompetitive mechanism of action. *J Biol Chem* 279: 29598-605, 2004.
36. Mahdipour E, Mace KA. Analyzing the angiogenic potential of Gr-1(+)CD11b (+) immature myeloid cells from murine wounds. *Methods Mol Biol* 916: 219-29, 2012.
37. Matono R, Miyano K, Kiyohara T, Sumimoto H. Arachidonic acid induces direct interaction of the p67(phox)-Rac complex with the phagocyte oxidase Nox2, leading to superoxide production. *J Biol Chem* 289: 24874-84, 2014.
38. Matsushita S, Nitanda T, Furukawa T, Sumizawa T, Tani A, Nishimoto K, Akiba S, Miyadera K, Fukushima M, Yamada Y, Yoshida H, Kanzaki T, Akiyama S. The effect of a thymidine phosphorylase inhibitor on angiogenesis and apoptosis in tumors. *Cancer Res* 59: 1911-6, 1999.
39. Menden H, Tate E, Hogg N, Sampath V. LPS-mediated endothelial activation in pulmonary endothelial cells: role of Nox2-dependent IKK-beta phosphorylation. *Am J Physiol Lung Cell Mol Physiol* 304: L445-55, 2013.
40. Menden H, Welak S, Cossette S, Ramchandran R, Sampath V. Lipopolysaccharide (LPS)-mediated angiopoietin-2-dependent autocrine angiogenesis is regulated by

NADPH oxidase 2 (Nox2) in human pulmonary microvascular endothelial cells. *J Biol Chem* 290: 5449-61, 2015.
41. Meng D, Mei A, Liu J, Kang X, Shi X, Qian R, Chen S. NADPH oxidase 4 mediates insulin-stimulated HIF-1alpha and VEGF expression, and angiogenesis in vitro. *PLoS One* 7: e48393, 2012.
42. Miyadera K, Sumizawa T, Haraguchi M, Yoshida H, Konstanty W, Yamada Y, Akiyama S. Role of thymidine phosphorylase activity in the angiogenic effect of platelet derived endothelial cell growth factor/thymidine phosphorylase. *Cancer Res* 55: 1687-90, 1995.
43. Morgan MJ, Liu ZG. Crosstalk of reactive oxygen species and NF-kappaB signaling. *Cell Res* 21: 103-15, 2011.
44. Naula CM, Logan FJ, Wong PE, Barrett MP, Burchmore RJ. A glucose transporter can mediate ribose uptake: definition of residues that confer substrate specificity in a sugar transporter. *J Biol Chem* 285: 29721-8, 2010.
45. Pendyala S, Gorshkova IA, Usatyuk PV, He D, Pennathur A, Lambeth JD, Thannickal VJ, Natarajan V. Role of Nox4 and Nox2 in hyperoxia-induced reactive oxygen species generation and migration of human lung endothelial cells. *Antioxid Redox Signal* 11: 747-64, 2009.
46. Peshavariya HM, Chan EC, Liu GS, Jiang F, Dusting GJ. Transforming growth factor-beta1 requires NADPH oxidase 4 for angiogenesis in vitro and in vivo. *J Cell Mol Med* 18: 1172-83, 2014.
47. Pugh CW, Ratcliffe PJ. Regulation of angiogenesis by hypoxia: role of the HIF system. *Nat Med* 9: 677-84, 2003.
48. Pugmire MJ, Ealick SE. Structural analyses reveal two distinct families of nucleoside phosphorylases. *Biochem J* 361: 1-25, 2002.
49. Pula G, Garonna E, Dunn WB, Hirano M, Pizzorno G, Campanella M, Schwartz EL, El Kouni MH, Wheeler-Jones CP. Paracrine stimulation of endothelial cell motility and angiogenesis by platelet-derived deoxyribose-1-phosphate. *Arterioscler Thromb Vasc Biol* 30: 2631-8, 2010.
50. Pula G, Mayr U, Evans C, Prokopi M, Vara DS, Yin X, Astroulakis Z, Xiao Q, Hill J, Xu Q, Mayr M. Proteomics identifies thymidine phosphorylase as a key regulator of the angiogenic potential of colony-forming units and endothelial progenitor cell cultures. *Circ Res* 104: 32-40, 2009.
51. Qutub AA, Popel AS. Reactive oxygen species regulate hypoxia-inducible factor 1alpha differentially in cancer and ischemia. *Mol Cell Biol* 28: 5106-19, 2008.
52. Ray PD, Huang BW, Tsuji Y. Reactive oxygen species (ROS) homeostasis and redox regulation in cellular signaling. *Cell Signal* 24: 981-90, 2012.
53. Renard P, Ernest I, Houbion A, Art M, Le Calvez H, Raes M, Remacle J. Development of a sensitive multi-well colorimetric assay for active NFkappaB. *Nucleic Acids Res* 29: E21, 2001.
54. Rey FE, Cifuentes ME, Kiarash A, Quinn MT, Pagano PJ. Novel competitive inhibitor of NAD(P)H oxidase assembly attenuates vascular O(2)(-) and systolic blood pressure in mice. *Circ Res* 89: 408-14, 2001.
55. Ronicke V, Risau W, Breier G. Characterization of the endothelium-specific murine vascular endothelial growth factor receptor-2 (Flk-1) promoter. *Circ Res* 79: 277-85, 1996.

56. Schreck R, Rieber P, Baeuerle PA. Reactive oxygen intermediates as apparently widely used messengers in the activation of the NF-kappa B transcription factor and HIV-1. *EMBO J* 10: 2247-58, 1991.
57. Schroder K, Zhang M, Benkhoff S, Mieth A, Pliquett R, Kosowski J, Kruse C, Luedike P, Michaelis UR, Weissmann N, Dimmeler S, Shah AM, Brandes RP. Nox4 is a protective reactive oxygen species generating vascular NADPH oxidase. *Circ Res* 110: 1217-25, 2012.
58. Sengupta S, Sellers LA, Matheson HB, Fan TP. Thymidine phosphorylase induces angiogenesis in vivo and in vitro: an evaluation of possible mechanisms. *Br J Pharmacol* 139: 219-31, 2003.
59. Skindersoe ME, Kjaerulff S. Comparison of three thiol probes for determination of apoptosis-related changes in cellular redox status. *Cytometry A* 85: 179-87, 2014.
60. Takakura Y, Kuentzel SL, Raub TJ, Davies A, Baldwin SA, Borchardt RT. Hexose uptake in primary cultures of bovine brain microvessel endothelial cells. I. Basic characteristics and effects of D-glucose and insulin. *Biochim Biophys Acta* 1070: 1-10, 1991.
61. Tobe M, Isobe Y, Tomizawa H, Nagasaki T, Takahashi H, Fukazawa T, Hayashi H. Discovery of quinazolines as a novel structural class of potent inhibitors of NF-kappa B activation. *Bioorg Med Chem* 11: 383-91, 2003.
62. Toi M, Atiqur Rahman M, Bando H, Chow LW. Thymidine phosphorylase (platelet-derived endothelial-cell growth factor) in cancer biology and treatment. *Lancet Oncol* 6: 158-66, 2005.
63. Tojo T, Ushio-Fukai M, Yamaoka-Tojo M, Ikeda S, Patrushev N, Alexander RW. Role of gp91phox (Nox2)-containing NAD(P)H oxidase in angiogenesis in response to hindlimb ischemia. *Circulation* 111: 2347-55, 2005.
64. Tozzi MG, Camici M, Mascia L, Sgarrella F, Ipata PL. Pentose phosphates in nucleoside interconversion and catabolism. *FEBS J* 273: 1089-101, 2006.
65. Ushio-Fukai M, Nakamura Y. Reactive oxygen species and angiogenesis: NADPH oxidase as target for cancer therapy. *Cancer Lett* 266: 37-52, 2008.
66. Vara D, Campanella M, Pula G. The novel NOX inhibitor 2-acetylphenothiazine impairs collagen-dependent thrombus formation in a GPVI-dependent manner. *Br J Pharmacol* 168: 212-24, 2013.
67. Vara DS, Campanella M, Canobbio I, Dunn WB, Pizzorno G, Hirano M, Pula G. Autocrine amplification of integrin alphaIIbbeta3 activation and platelet adhesive responses by deoxyribose-1-phosphate. *Thromb Haemost* 109: 1108-19, 2013.
68. Vigont V, Kolobkova Y, Skopin A, Zimina O, Zenin V, Glushankova L, Kaznacheyeva E. Both Orai1 and TRPC1 are Involved in Excessive Store-Operated Calcium Entry in Striatal Neurons Expressing Mutant Huntingtin Exon 1. *Front Physiol* 6: 337, 2015.
69. Wang J, Hong Z, Zeng C, Yu Q, Wang H. NADPH oxidase 4 promotes cardiac microvascular angiogenesis after hypoxia/reoxygenation in vitro. *Free Radic Biol Med* 69: 278-88, 2014.
70. Wei Y, Gong J, Xu Z, Duh EJ. Nrf2 promotes reparative angiogenesis through regulation of NADPH oxidase-2 in oxygen-induced retinopathy. *Free Radic Biol Med* 99: 234-243, 2016.
71. Zafarullah M, Li WQ, Sylvester J, Ahmad M. Molecular mechanisms of N-acetylcysteine actions. *Cell Mol Life Sci* 60: 6-20, 2003.

ABBREVIATION LIST

Biotinyl-iodoacetamide (BIAM)
3-methoxycarbonyl-2,2,5,5-tetramethylpyrrolidine (CMH)
4′,6-diamidino-2-phenylindole (DAPI)
Deoxyribose-1-phosphate (dRP)
Diphenylene iodonium (DPI)
Electron paramagnetic resonance (EPR)
2,7-dichlorodihydrofluorescein diacetate (H2-DCFDA)
Fluorescein Isothiocyanate (FITC)
Glucose transporter 1 (GLUT1)
Horseradish peroxidase (HRP)
Human umbilical vein endothelial cells (HUVECs)
Hypoxia-induced factor 1 (HIF1)
Inhibitor of NF-κB (IκB)
Lipopolysaccharide (LPS)
Mn(III)tetrakis(4-benzoic acid)porphyrin (MnTBAP)
N-acetyl-L-cysteine (NAC)
NADPH oxidase (NOX)
Nuclear factor kappa B (NF-κB)
Nuclear factor erythroid 2–related factor 2 (Nrf-2)
N4-[2-(4-phenoxyphenyl)ethyl]-4,6-quinazolinediamine (QNZ)
Reactive oxygen species (ROS)
Sodium Dodecyl Sulfate Polyacrylamide Gel Electrophoresis (SDS-PAGE)
Superoxide dismutase (SOD)
Thymidine phosphorylase (TP)
Vascular endothelial growth factor (VEGF)
VEGF receptor 2 (VEGFR2)

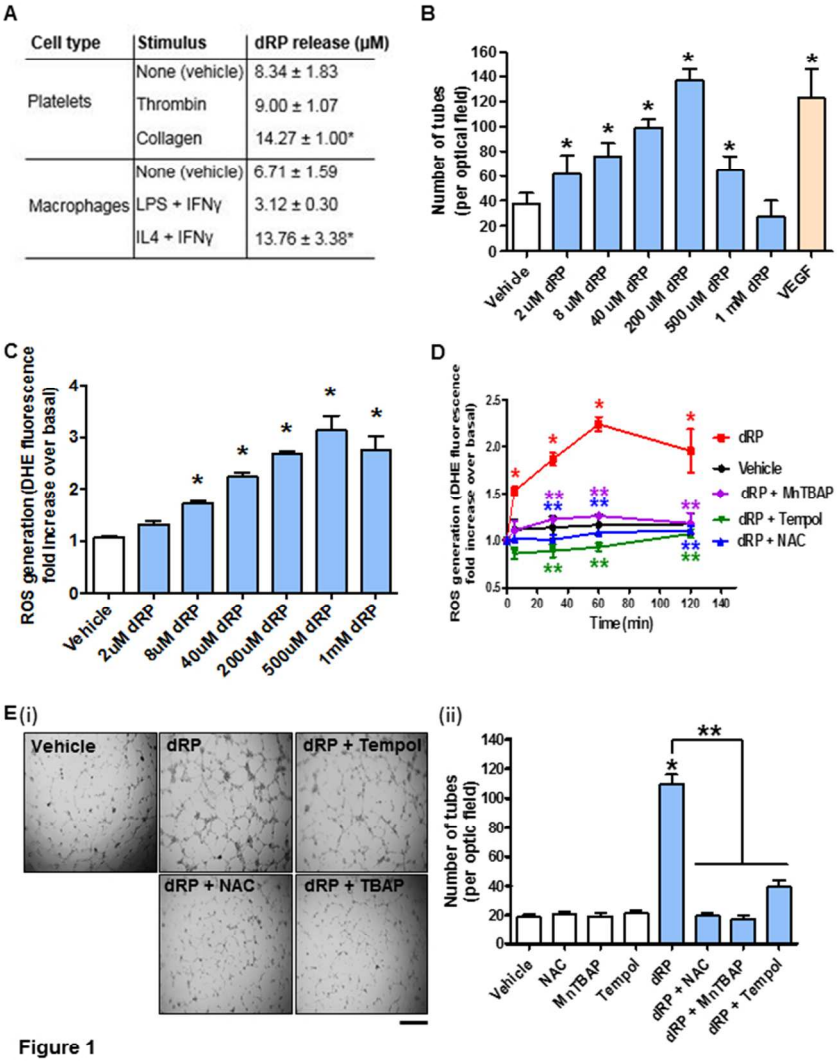

Figure 1

Figure 1. dRP stimulates angiogenesis and oxidative stress of endothelial cells in vitro. (A) The concentration of dRP released by human platelets and mouse macrophages in vitro was quantified by LC-MS. Presented data are from 6 and 3 independent samples, respectively. Statistical significance was assessed by one-way ANOVA with Bonferroni post-hoc test (* = $p<0.01$ compared to non-stimulated platelets). (B-) HUVECs were seeded at a density of 3 x 102 cells/mm2 on growth factor-reduced Matrigel® and cultured in basal medium (no FBS). Different concentrations of dRP between 2µM and 1mM and (after 4 hours of culture, quantification of tube number per optical field was performed using the Angiogenesis Analyzer plugin of ImageJ. (C) ROS generation was analysed with DHE staining for 1 hour in response to concentrations of dRP ranging from 2µM to 1mM and expressed as fold-increase over basal. (D) Time course of ROS generation in response to 200µM dRP in the presence of ROS scavengers 1mM NAC, 10µM MnTBAP or 10µM Tempol) or vehicle. ROS production was assessed after 5, 30, 60 and 120 minutes and expressed as fold-increase over basal. (E) HUVECs were seeded at a density of 3 x 102 cells/mm2 on growth factor-reduced Matrigel® and cultured in basal medium (no FBS). 200µM dRP was incubated in the presence or absence of 1mM NAC,

10μM Tempol or 10μM MnTBAP. After 4 hours of culture, quantification of tube number per optical field was performed using the Angiogenesis Analyzer plugin of ImageJ. Representative pictures are shown in (i) and quantification is shown in (ii). Throughout the figure, data are expressed as mean ± SEM and analyzed by one-way ANOVA (B and C, n=6; E, n=8) or two-way ANOVA (D, n=6). In either case, Bonferroni post-hoc test was used to identify statistically significant difference between conditions; * = $p<0.05$ compared to vehicle, ** = $p<0.05$ compared to dRP). (E) Bars = 300μm.

190x254mm (96 x 96 DPI)

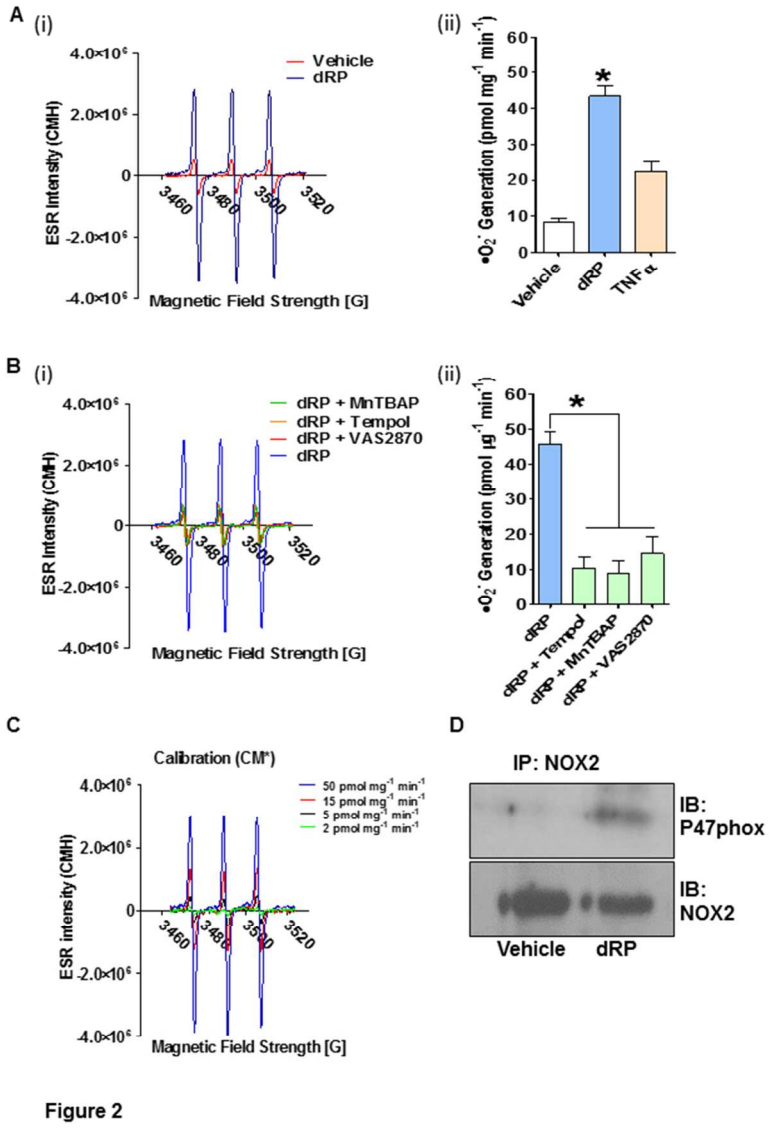

Figure 2

Figure 2. dRP stimulates increased levels of ROS generation in HUVECs in a NOX-dependent manner. Quantitative measurements of superoxide anion production in HUVECs was performed using the cell-permeable superoxide-specific spin probe CMH and EPR. (A) Cells were treated for 45 minutes with 200µM dRP, vehicle (Tyrode's HEPES buffer) or 50ng/ml TNF-α in the presence of CMH (200µM) before EPR analysis. (B) Inhibition of superoxide anion production induced by 200µM dRP was also detected by EPR by 10µM MnTBAP, 10µM Tempol or 1µM VAS2870. For A and B, representative EPR traces are shown in (i). The bar charts in (ii) show superoxide anion production rates (pmol mg−1 min−1) (mean ± SEM, one-way ANOVA with Bonferroni post-hoc test, * = $p<0.05$, n=4). (C) Calibration curve obtained using known concentrations of the oxidized spin probe (i.e. CM*). (D) Activation of NOX2 confirmed by co-immunoprecipitation with p47phox. HUVECs were treated with a vehicle or 200µM dRP for 1 hour. NOX2 immunoprecipitates were subjected to immunoblotting for p47phox and NOX2. Blots are representative of 4 independent experiments.

190x254mm (96 x 96 DPI)

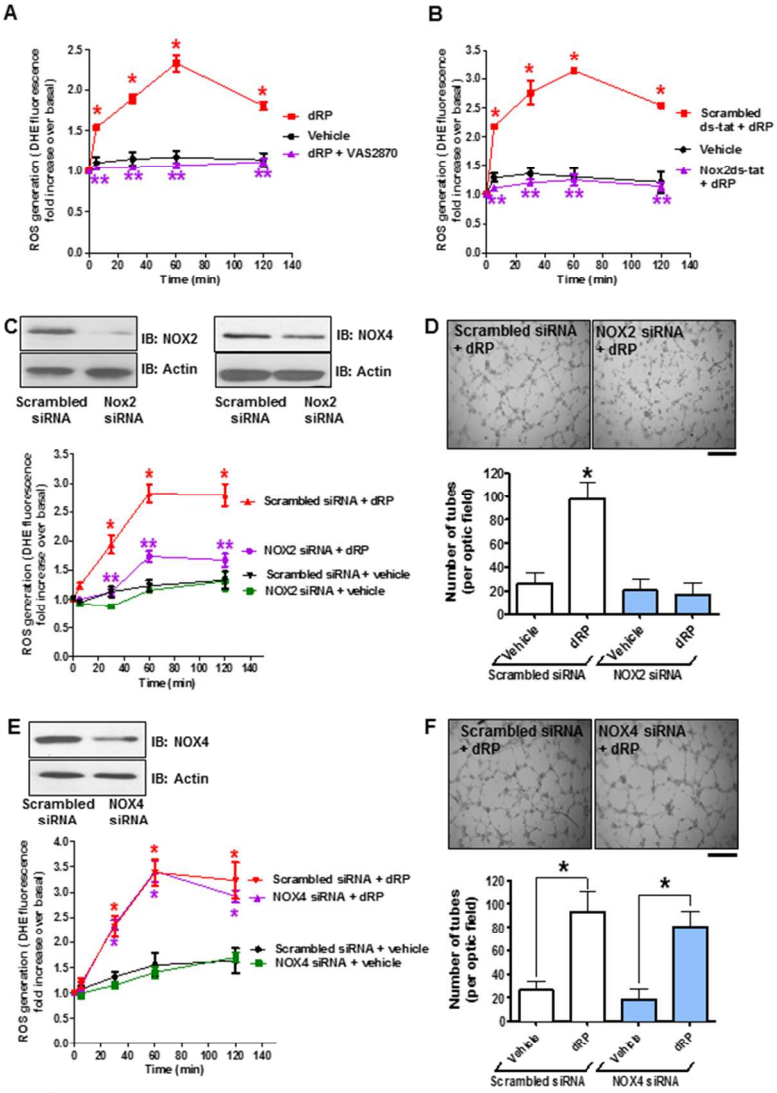

Figure 3

Figure 3. dRP stimulates increased levels of ROS generation and tube formation in a NOX-dependent manner. (A) ROS generation in response to 200μM dRP or vehicle was measured as described above in the presence of 1μM VAS2870. (B) dRP-induced ROS production resulted suppressed by inhibition of NOX2 with 10μM Nox2ds-tat. Immunoblot analysis of NOX2-specific knock down by siRNA (and scrambled siRNA control). (C) ROS generation in response to 200μM dRP was measured in control (scrambled siRNA) and NOX2 knockdown cells. (D) Representative images of tube formation by cells transfected with scrambled siRNA and NOX2 siRNA in the presence of 200μM dRP are shown. Total number of tubes was measured with the Angiogenesis Analyzer plugin of ImageJ. Representative images (top) and data analysis are shown (bottom). (E-F) Genetic silencing of NOX4 in HUVECs does not affect dRP-induced ROS generation increase. Tube formation in response to 200μM dRP by scrambled and NOX4 knockdown cells was measured. Time courses in A, B , C and E were analysed by two-way ANOVA (n=4) with Bonferroni post-hoc test (* = $p<0.05$, compared to vehicle in A and B or vehicle/scrambled siRNA in C and E; ** = $p<0.05$ compared to dRP in A and B or dRP/scrambled siRNA in C and E). Bar graphs in D and F represent quantification of tube

number per optical field compared by one-way ANOVA with Bonferroni post-test (* = $p<0.05$ compared to vehicle, n = 5). Bar: (D and F) 300μm.

190x254mm (96 x 96 DPI)

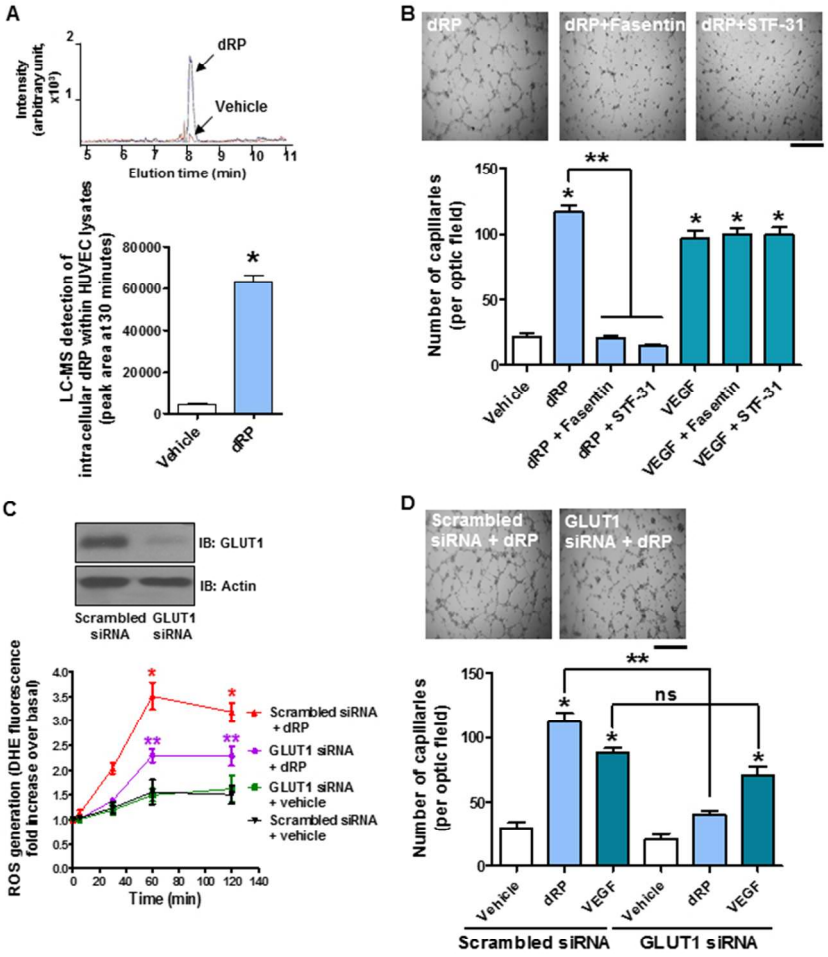

Figure 4

Figure 4. dRP acts intracellularly following its internaliszation by the transporter GLUT1. (A) LC-MS detection of intracellular dRP. HUVECs were treated with 200µM dRP, before 3 washes in PBS and ultrasonication. Example chromatogram (upper panel) and data quantification (lower panel) are shown. Statistical significance was tested by t-test (* = $p<0.05$, compared to vehicle, n=4). (B) STF-31 and fasentin (10µM) inhibited dRP- but not VEGF-dependent tube formation. Example pictures (upper panel) and data quantification (lower panel) are shown. Bar graphs represent quantification of tube number per optical field compared by one-way ANOVA with Bonferroni post-hoc test (* = $p<0.05$ compared to vehicle, n = 5). Bar: 300µm. (C) siRNA-dependent silencing of GLUT1 inhibits dRP-induced ROS generation. Following GLUT1 silencing displayed in top panels, ROS was measured as described over a period of two hours. Time courses were analysed by two-way ANOVA (n=4) with Bonferroni post-hoc test (* = $p<0.05$, compared to vehicle/scrambled siRNA; ** = $p<0.05$ compared to dRP/scrambled siRNA). (D) siRNA-dependent silencing of GLUT1 inhibits dRP-induced tube formation. Example pictures for dRP response by HUVECs treated with scrambled siRNA or GLUT1 siRNA are shown in top panels. Bar graphs represent quantification of tube

number per optical field compared by one-way ANOVA with Bonferroni post-hoc test (* = $p<0.05$ compared to scrambled siRNA/vehicle, ** = $p<0.05$ compared to scrambled siRNA/dRP, ns = non significant, n = 4). Bar: 300µm.

190x254mm (96 x 96 DPI)

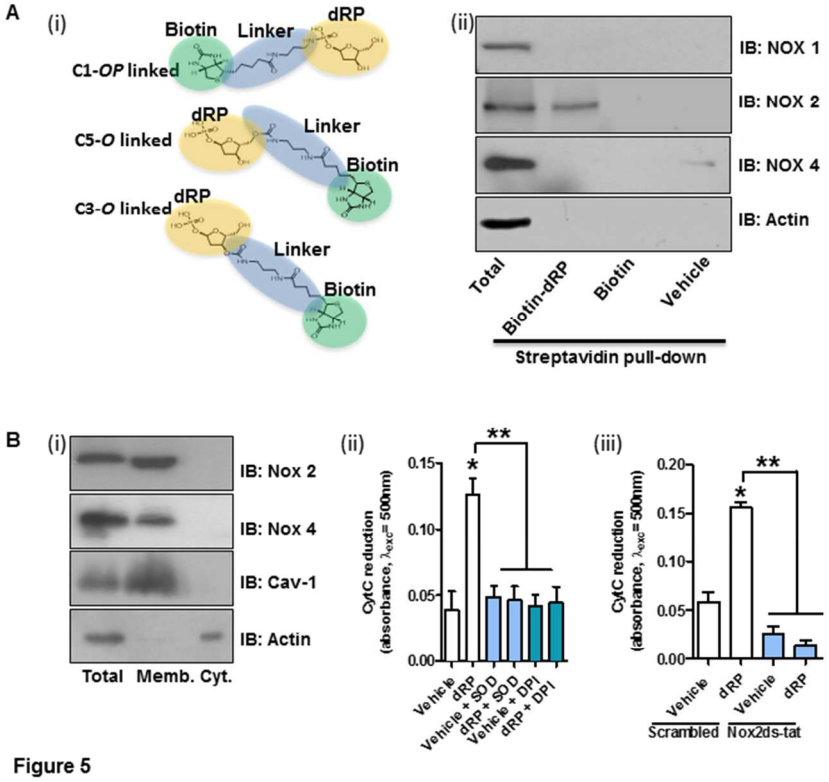

Figure 5

Figure 5. dRP directly activates NOX2. (A) Binding of NOX2 was assessed by pull-down using a mixture of three dRP-biotin conjugates (i). NOX 1, 2, 4, and actin were detected by immunoblotting (ii) (4 independent experiments). (B) Membrane fractions treated with dRP display NOX activation. NOX-1, 2, 4, Caveolin-1 and β-actin were tested by immunoblotting (i). The membrane fractions were treated with 200μM dRP using cytochrome c reduction assay. Cytochrome c reduction was measured as absorbance at wavelength 550nm. 1000 U/mL SOD was utilized to determine the superoxide anion-dependent component, while DPI (100μM) was used to determine the role of NOXs and other flavoenzymes (ii). 10μM Nox2ds-tat (or scrambled peptide as a negative control) was utilised to assess the role of NOX2 in the oxidative response measured by this membrane assay (iii). Data in B were analysed by one-way ANOVA with Bonferroni post-test (* = $p<0.05$, compared to vehicle (ii) or scrambled siRNA/vehicle (iii), ** = $p<0.05$ compared to dRP (ii) or scrambled siRNA/dRP (iii), n=6).

190x254mm (96 x 96 DPI)

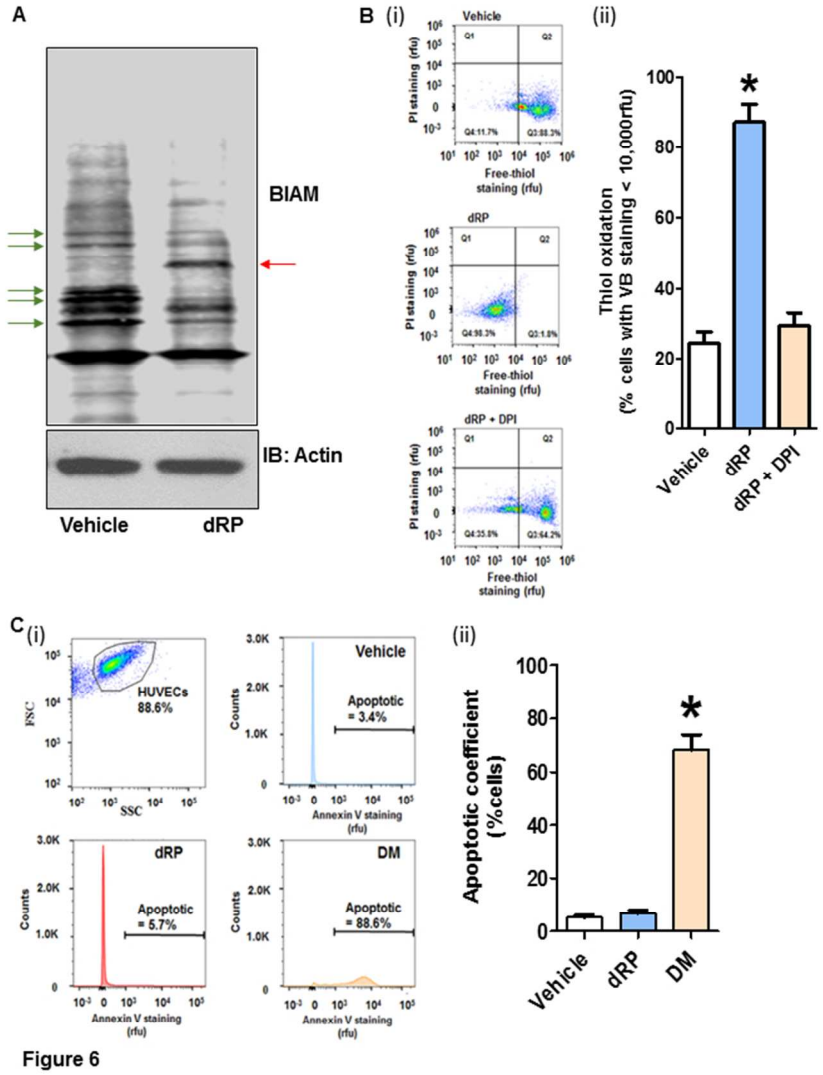

Figure 6

Figure 6. dRP induces oxidative stress without significantly increasing apoptosis. (A) HUVECs treated with or without 200μM dRP for 4 hours were labelled for 2 h with 20μM BIAM in anoxic conditions. Thiol oxidation status was determined by protein separation using SDS-PAGE and staining with HRP-streptavidin. Green arrows indicate thiol oxidation, whilst red arrows represent thiol reduction. β-actin immunoblotting was used to confirm equal loading. Blots are representative of 4 independent experiments. (B) VitaBright-43® staining was also utilized to measure the level of intracellular reduced thiols. HUVECs were treated with vehicle solution (Tyrode's HEPES buffer) or stimuli with/without NOX inhibitor (200μM dRP, 10μM DPI) for 30 min. Cells were co-stained with VitaBright-43® and propidium iodide and analysed by image cytometry using the NucleoCounter NC-3000® system. Plots show VitaBright-43® (VB) intensity versus propidium iodide intensity are shown (i). Intracellular thiol oxidation was quantified by counting the % of cells with VitaBright-43® staining below 10,000 rfu (ii). Statistical analysis was performed by one-way ANOVA with Bonferroni post-test (* = $p<0.05$, compared to vehicle, n=6). (B Cell apoptosis was measured by flow cytometry for PE-annexin V staining. HUVECs were treated with vehicle (Tyrode's HEPES buffer), 200μM dRP

or 5mM diethyl maleate (positive control) for 12 h. Forward scattering (FSC)/side scattering (SSC) and annexin V staining histograms from 4 independent experiments are presented (i). Data analysis is also shown (ii). Data are mean ± SEM analyzed by one-way ANOVA with Bonferroni post-test (* = $p<0.05$, compared to vehicle, n=6).

190x254mm (96 x 96 DPI)

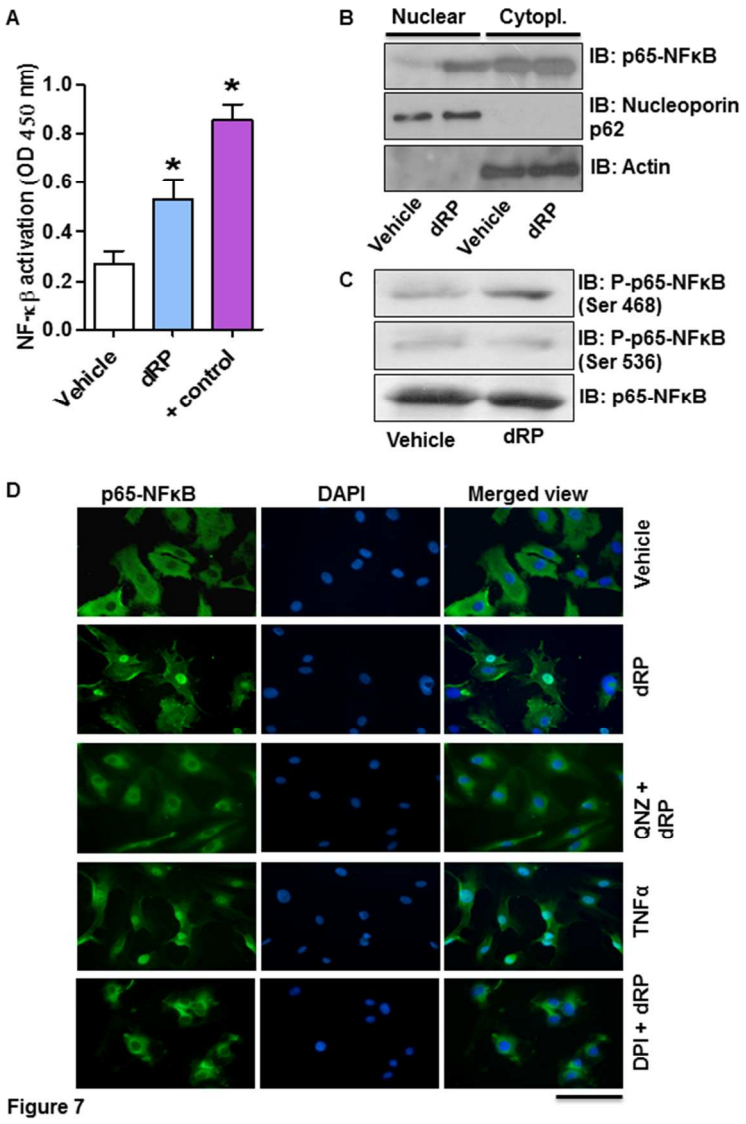

Figure 7

Figure 7. NF-κB is activated in response to dRP. (A) DNA-binding capacity of NF-κB (p65 subunit) was determined using TransAM® for NF-κB (Active Motif, cat. no. #43296). HUVECs were treated with or without 200μM dRP for 30 minutes. Whole cell extract from Jurkat cells stimulated with 12-O-tetradecanoylphorbol-13-acetate and calcium was used as positive control. One-way ANOVA with Bonferroni post-test was used to test statistical significance (mean ± SEM, n=6, * = $p<0.05$). (B) The translocation of p65-NF-κB to the nucleus was tested by subcellular fractionation using the NE-PER kit (Pierce). Cytoplasmic and nuclear fractions were immunoblotted for p65-NF-κB, nucleoporing-p62 (a nuclear marker) and β-actin (a cytoplasmic marker). Data are representative of 4 independent experiments. (C) NF-κB activation was also investigated by phospho-specific immunoblotting. Total cell lysate immunoblotted with phospho-specific NF-κB antibodies (Ser468 or Ser536) and total NF-κB antibody (as loading control). Immunoblots represent 4 independent experiments. (D) Immunolocalisation of p65-NF-κB (green) in dRP-stimulated HUVECs (200μM, 1 hour) was also tested. Where indicated, 100nM QNZ, an inhibitor of NF-κB activation, was added. 100μM DPI was used as a NOX inhibitor, whereas 50 ng/ml TNF-α was utilized as a positive control. Images

are representative of 5 independent experiments. Bar: (D) 100μm.

190x254mm (96 x 96 DPI)

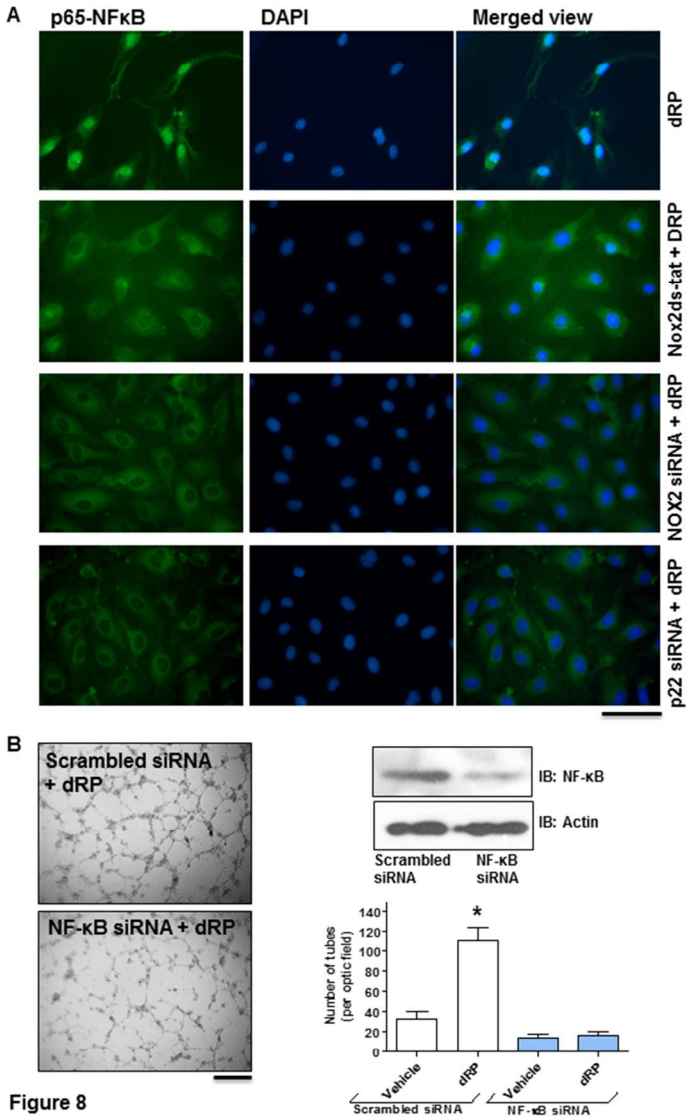

Figure 8

Figure 8. dRP induces NF-κB activation in a NOX-dependent manner and NF-κB activity is critical for endothelial tube formation in response to dRP. (A) Representative immunofluorescence images of HUVECs stained for NF-κB (green) and DAPI (blue). Where indicated, HUVECs were pre-treated with 10μM Nox2ds-tat peptide for 1 hour or subjected to NOX2 and p22phox siRNA-mediated genetic silencing for 72 h prior to treatment with 200μM dRP for 30 minutes. Images are representative of 4 independent experiments. (B) Tube formation was assessed by seeding scrambled and NF-κB siRNA-treated cells onto growth factor-reduced Matrigel® with or without 200μM dRP. Representative images show tube formation after 4 hours (left) and p65-NF-κB downregulation (right). Bar graphs (bottom right) represent quantification of tube number per optical field using ImageJ software with Angiogenesis Analyzer plugin (* = $p<0.05$, one-way ANOVA with Bonferroni post-test, n = 5). Bar: (A) 100μm; (B) 300μm.

190x254mm (96 x 96 DPI)

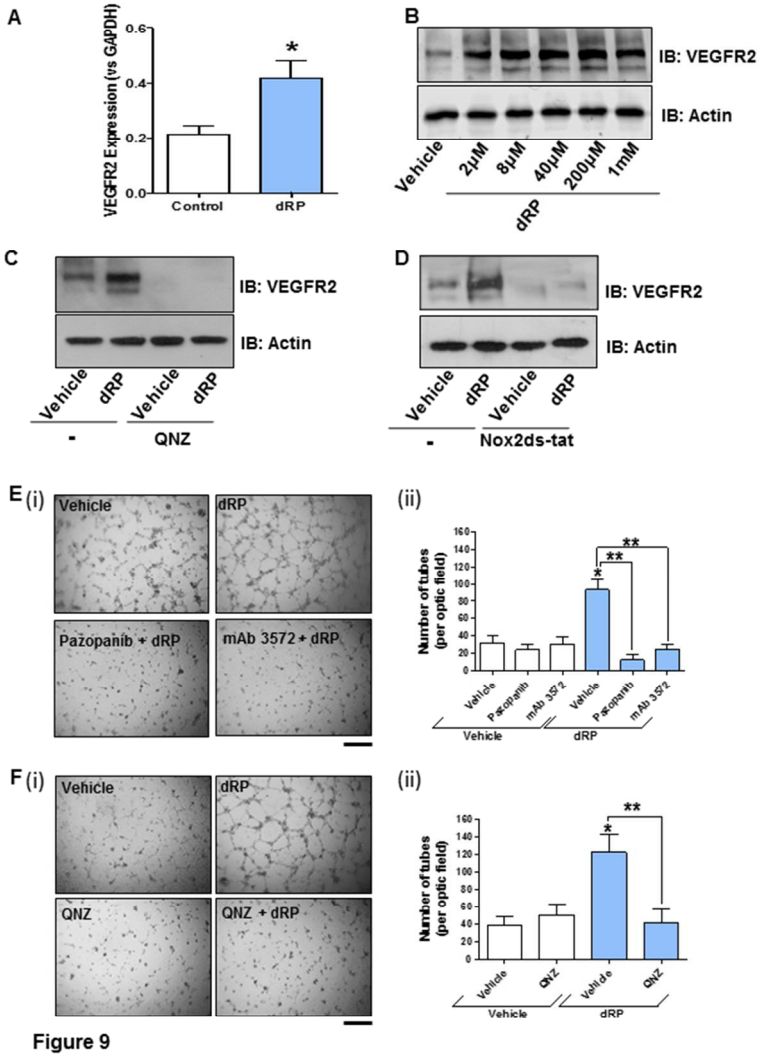

Figure 9

Figure 9. VEGFR2 is upregulated in response to dRP in a NF-κB-dependent manner and its activity is necessary for dRP-dependent angiogenesis. (A) qPCR analysis of VEGFR2 expression on HUVECs treated with or without 200μM dRP for 4 hours. The 2-ΔΔCt analysis method was used to analyse the data with GAPDH used as normalizer. Statistical significance of the difference was tested using non-parametric Mann-Whitney test (mean ± SEM, n=4, * = $p<0.05$). (B) HUVECs were treated with increasing concentration of dRP (2μM to 1mM) for 6 hours. Alternatively, HUVEC were incubated with (C) 100nM QNZ or (D) 10μM Nox2ds-tat for 1 hour and then stimulated with 200μM dRP for 6 hours. Cell lysates were immunoblotted for VEGFR2 and β-actin. Data are representative of 4 independent experiments. (E) Effects of VEGFR2 inhibitors Pazopanib and mAB3572 on dRP-induced tube formation. HUVECs with or without 200μM dRP were tested in the presence of 10 μg/ml Pazopanib and 50 ng/mL mAB3572 antibody. Representative pictures in (i) and quantification in (ii). (F) Effects of the NF-κB inhibitor QNZ (100nM) on dRP-induced tube formation. Representative pictures in (i) and quantification in (ii). Bar graphs represent quantification of tube number per optical field performed using ImageJ software with Angiogenesis Analyzer plugin and compared by one-

way ANOVA with Bonferroni post-test (* = $p<0.05$, n=6). Bar: (E and F) 300μm.

190x254mm (96 x 96 DPI)

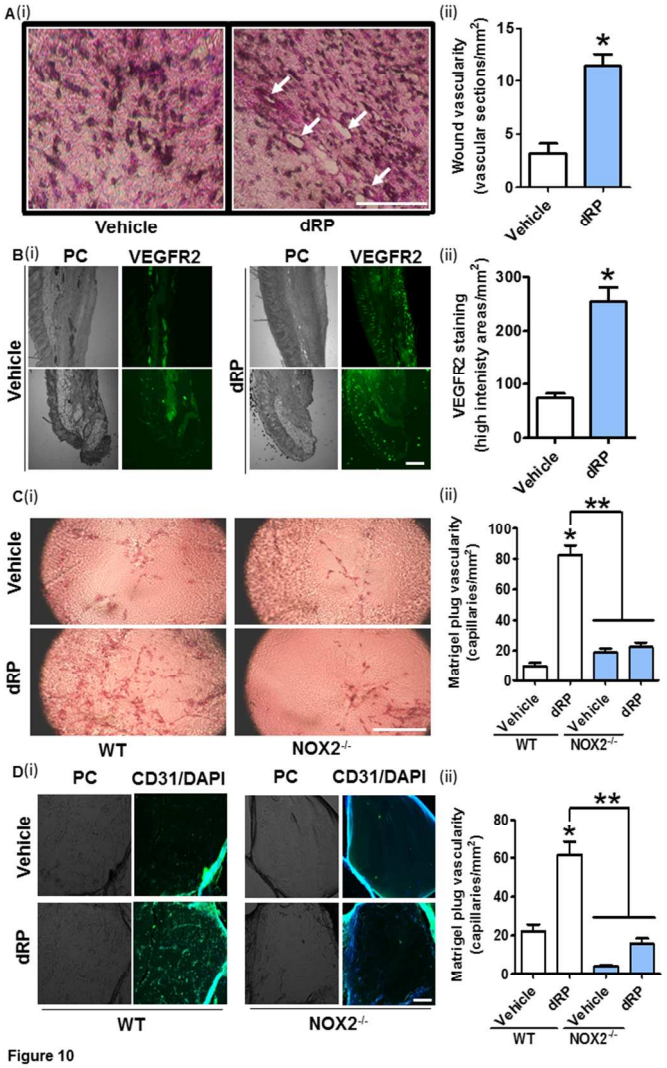

Figure 10

Figure 10. dRP stimulates VEGFR2 upregulation and NOX2-deoendent angiogenesis in vivo. (A) Representative examples (i) and quantification (ii) of the hematoxylin/eosin staining of wound tissue treated with dRP or vehicle control (PBS). Data represent counts of vascular structures (surrounded by continuous intimal monolayer) per optic field. Statistical significance of the difference was assessed by non-parametric Mann-Whitney test (* = $p<0.05$ compared to vehicle, n = 10). Vascular structures are highlighted by white arrows in the picture. (B) Representative examples (i) and quantification (ii) of the VEGFR2-specific staining of wound tissue treated with dRP or vehicle control (PBS). Data represent counts of high fluorescence intensity areas per mm2, as estimated using ImageJ. Statistical significance of the difference was assessed by non-parametric Mann-Whitney test (* = $p<0.05$ compared to vehicle, n = 8). (C) Representative examples (i) and quantification (ii) of the hematoxylin staining of Matrigel™ plugs containing dRP (41.2µg/plug) or vehicle control (PBS) after 7 days of implantation in wild type (C57BL6/J) or NOX2-/- (Jackson Laboratories B6.129S-Cybbtm1Din/J) mice. Data represent counts of capillary structures per mm2, as estimated using ImageJ. Statistical significance of the difference was assessed by one-way ANOVA with

Bonferroni post-hoc test (* = p<0.05 compared to vehicle, ** = p<0.05 compared to dRP, n=6). (D) Representative examples (i) and quantification (ii) of the DAPI/CD31-specific staining of Matrigel™ plugs containing dRP (41.2µg/plug) or vehicle control (PBS) after 7 days of implantation in wild type (C57BL6/J) or NOX2-/- (Jackson Laboratories B6.129S-Cybbtm1Din/J) mice. Data represent counts of capillary structures per mm2, as estimated using ImageJ. Statistical significance of the difference was assessed by one-way ANOVA with Bonferroni post-hoc test (* = p<0.05 compared to vehicle, ** = p<0.05 compared to dRP, n=6).Bars: 300µm (throughout).

190x338mm (96 x 96 DPI)

Original immunoblot files

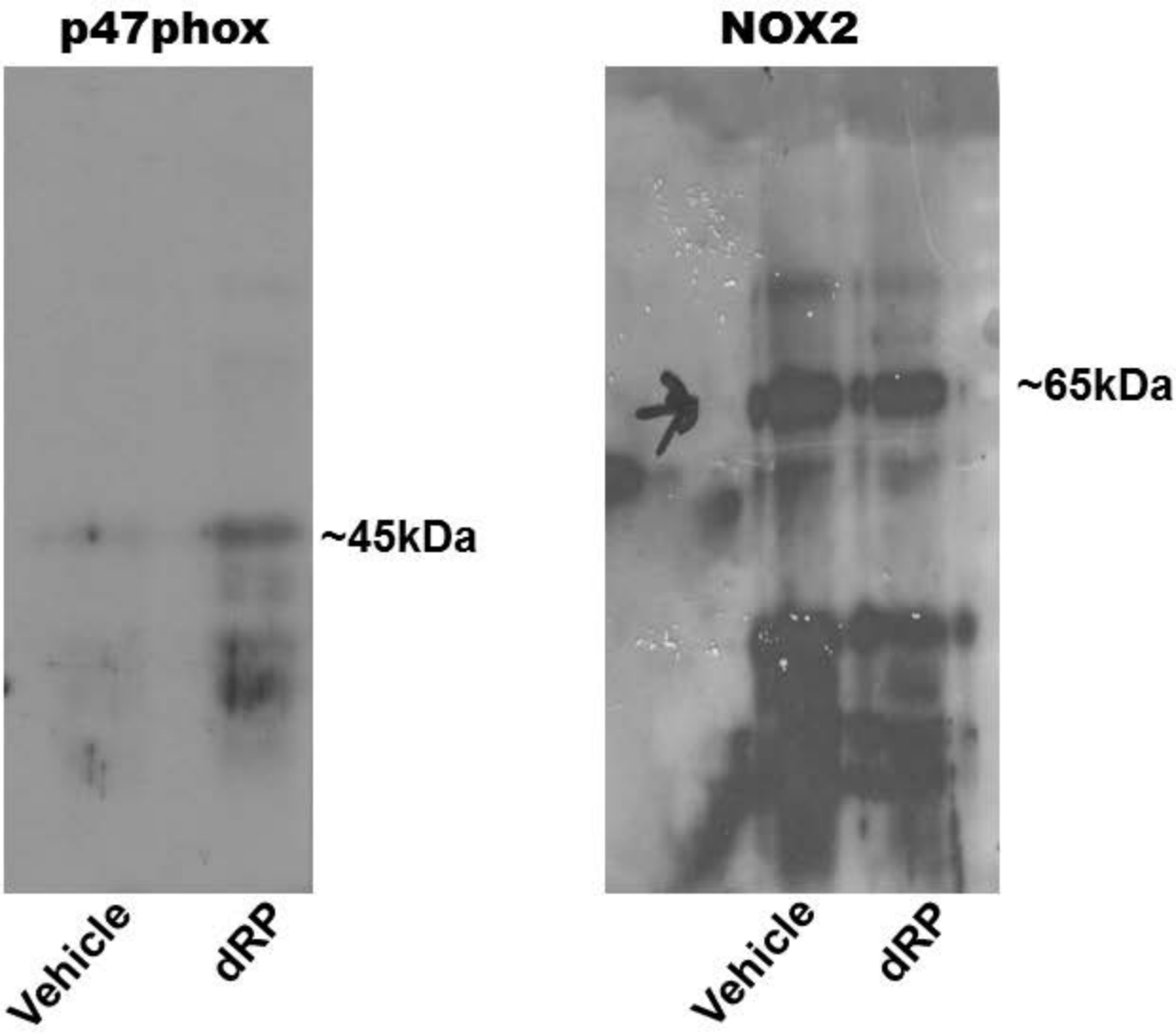

Figure 2D

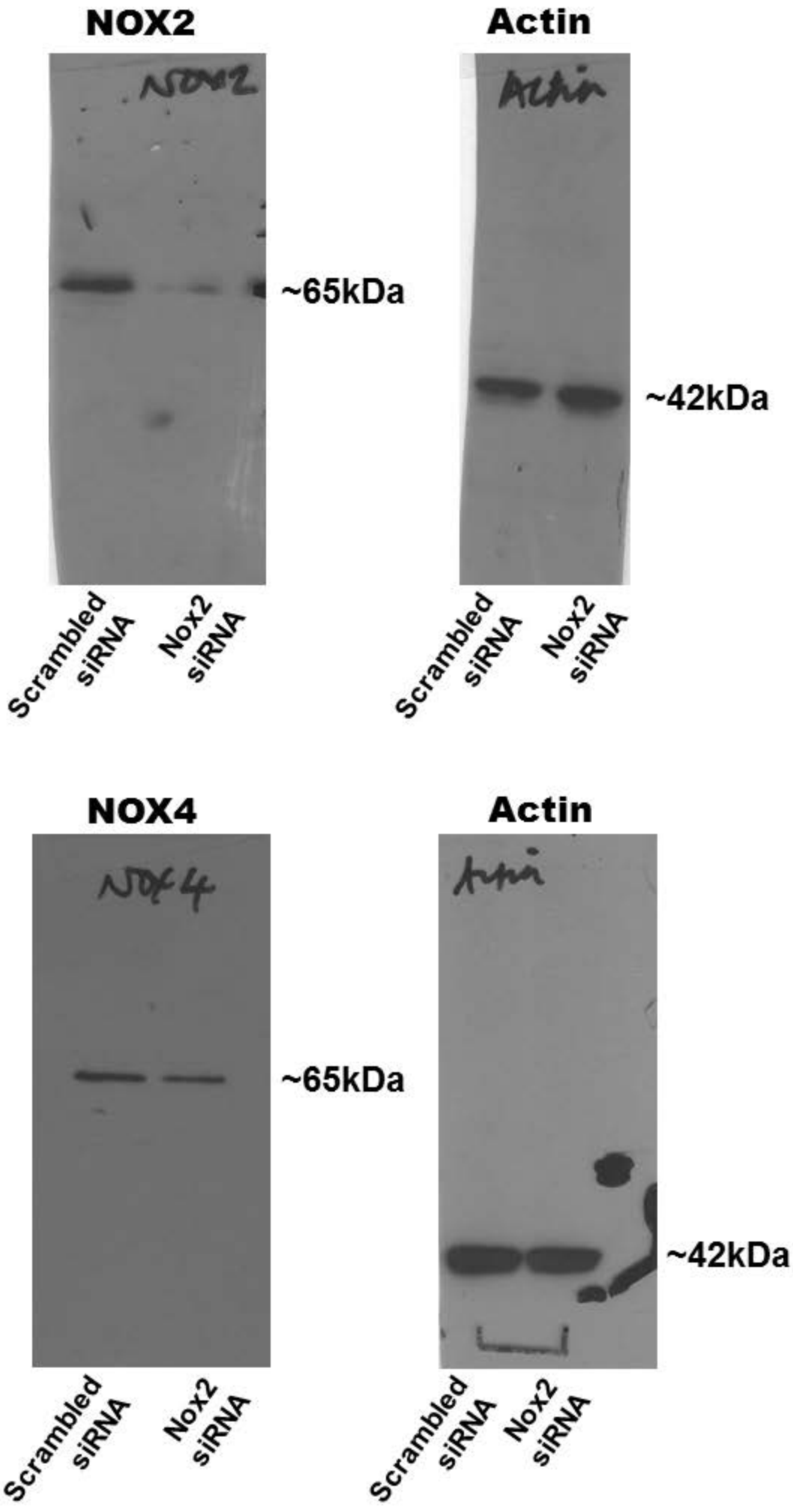
NOX2
Actin
~65kDa
~42kDa
Scrambled siRNA
Nox2 siRNA
Scrambled siRNA
Nox2 siRNA
NOX4
Actin
~65kDa
~42kDa
Scrambled siRNA
Nox2 siRNA
Scrambled siRNA
Nox2 siRNA

Figure 3C

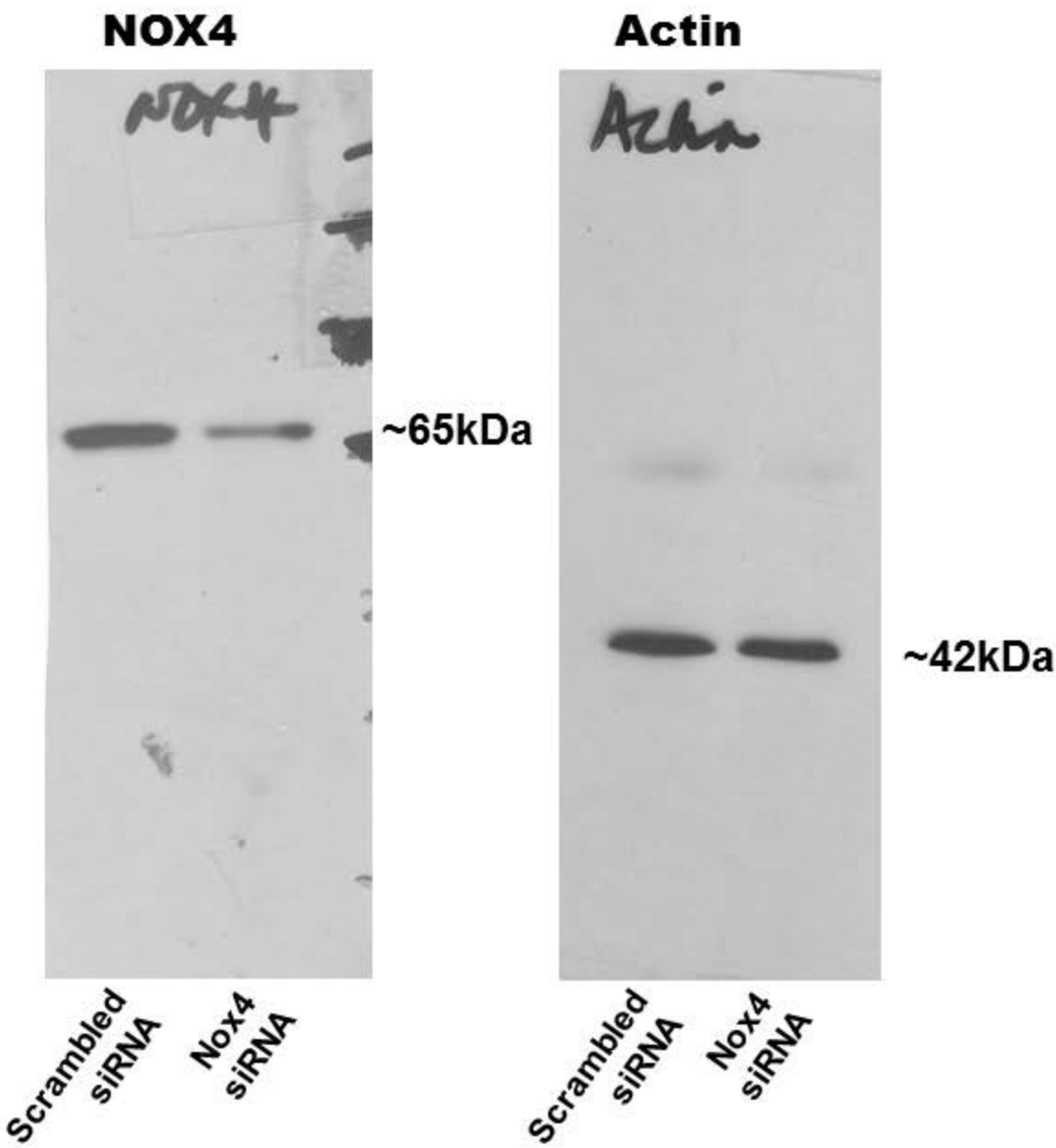
NOX4
Actin
~65kDa
~42kDa
Scrambled siRNA
Nox4 siRNA
Scrambled siRNA
Nox4 siRNA

Figure 3E

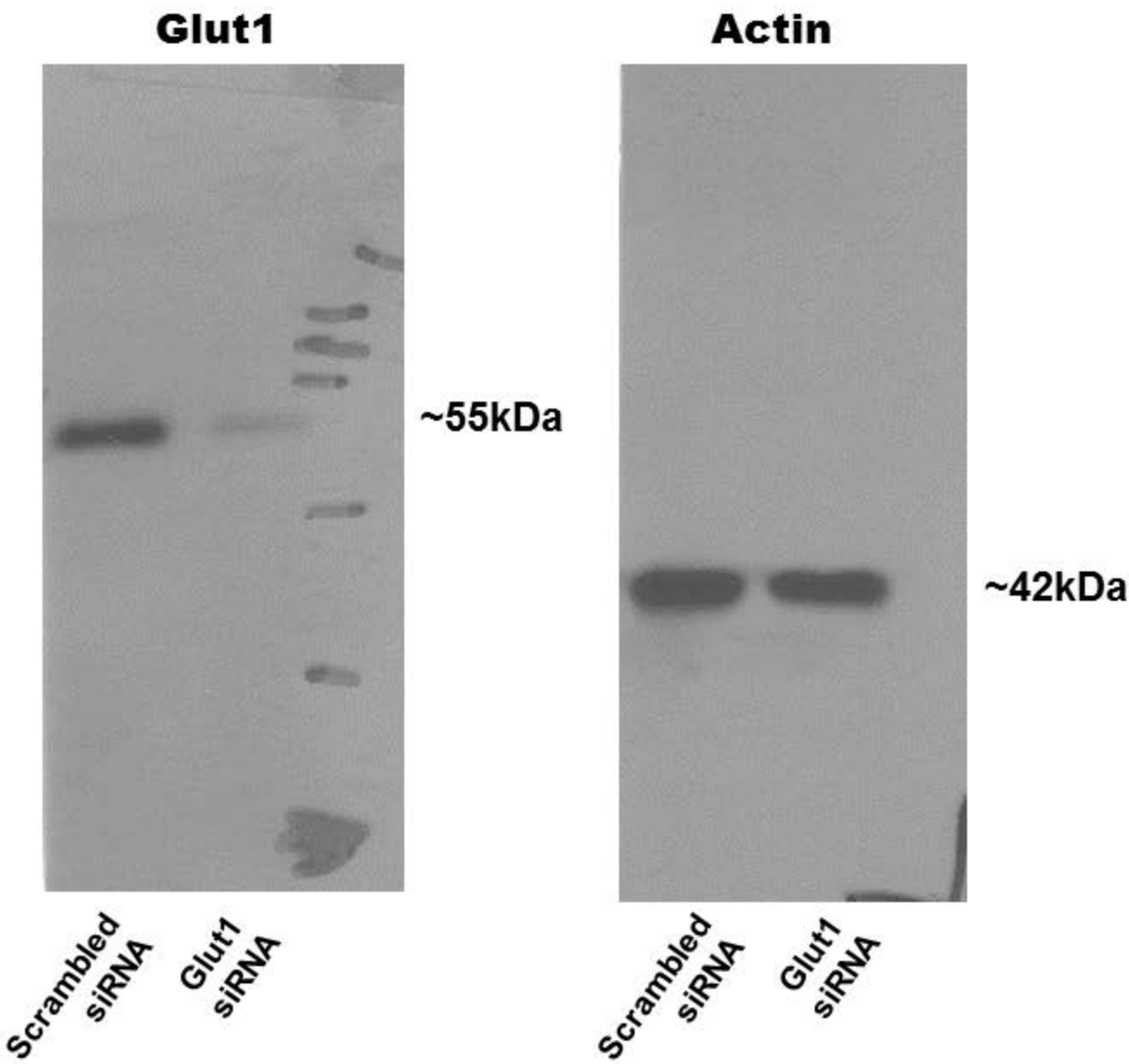
Glut1
Actin
~55kDa
~42kDa
Scrambled siRNA
Glut1 siRNA
Scrambled siRNA
Glut1 siRNA

Figure 4C

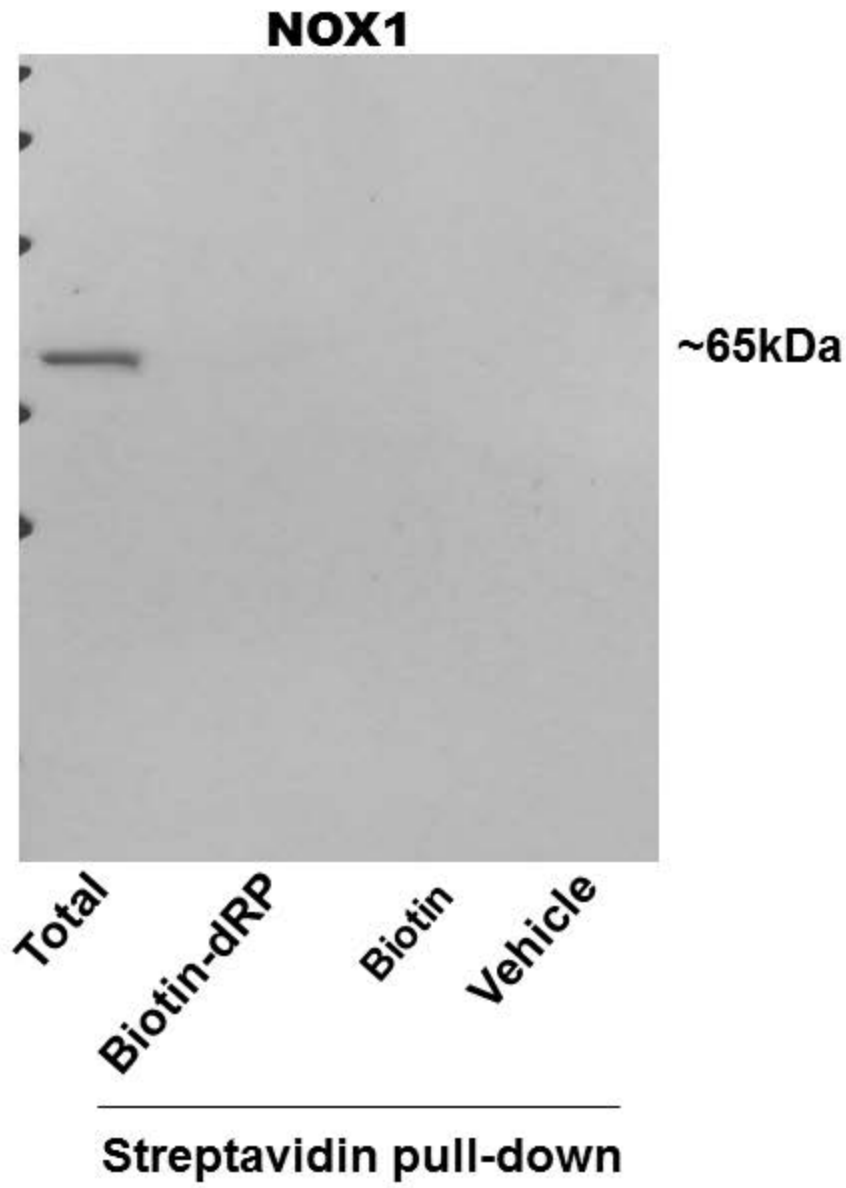
NOX1
~65kDa
Total
Biotin-dRP
Biotin
Vehicle
Streptavidin pull-down
NOX2
~65kDa
Total
Biotin-dRP
Biotin
Vehicle
Streptavidin pull-down

Figure 5A

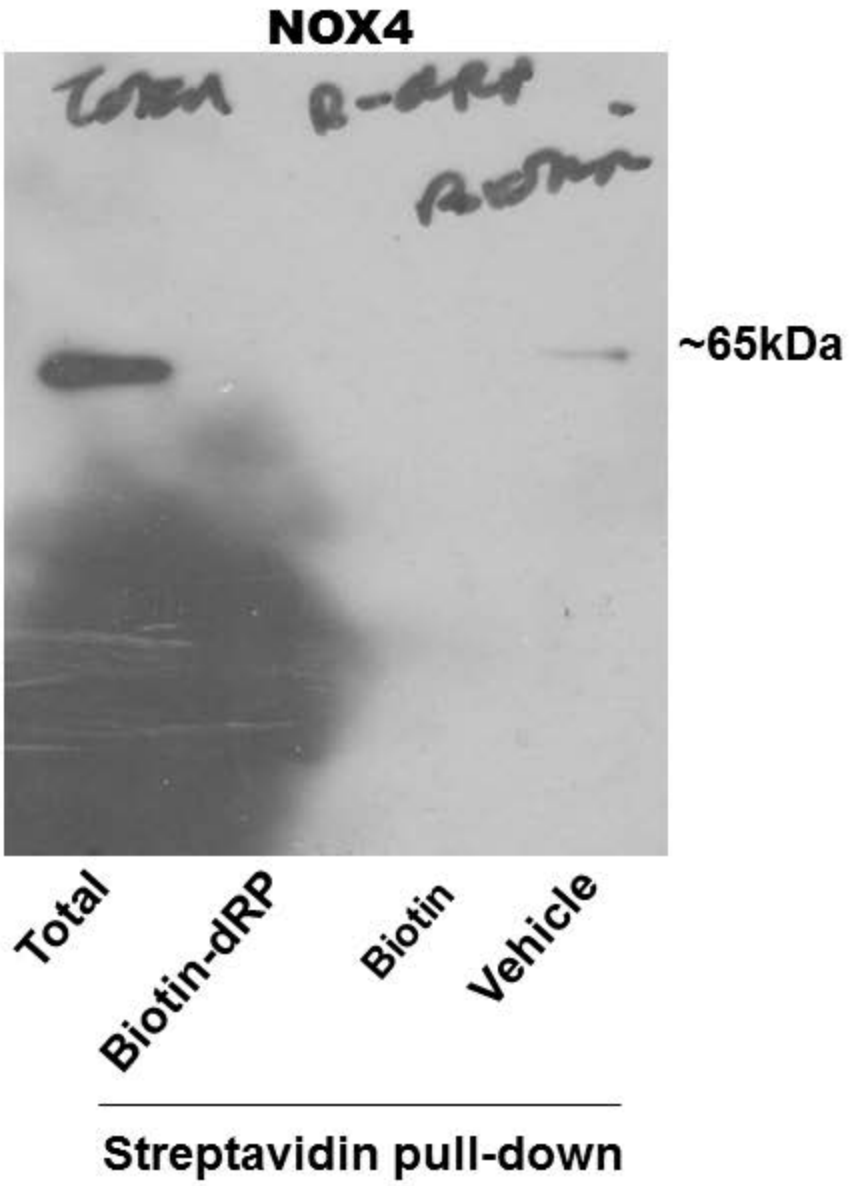
NOX4
~65kDa
Total
Biotin-dRP
Biotin
Vehicle
Streptavidin pull-down
Actin
~45kDa
Total
Biotin-dRP
Biotin
Vehicle
Streptavidin pull-down

Figure 5A

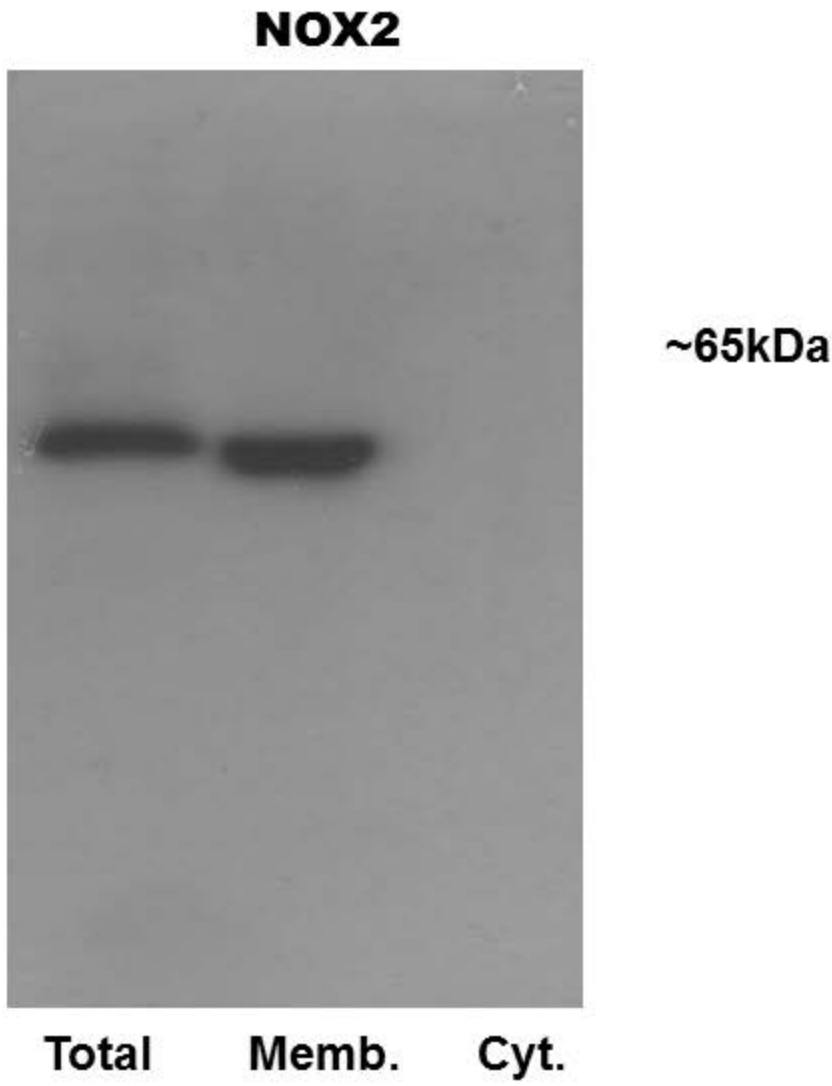

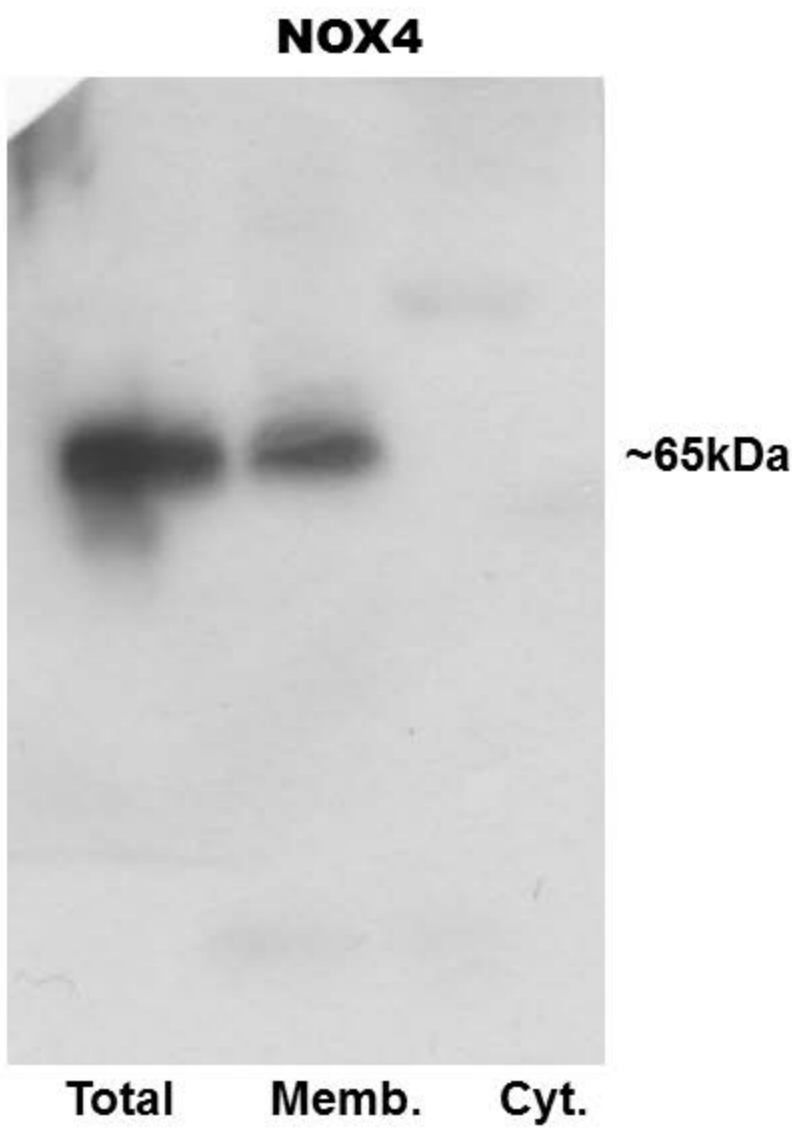

Figure 5B

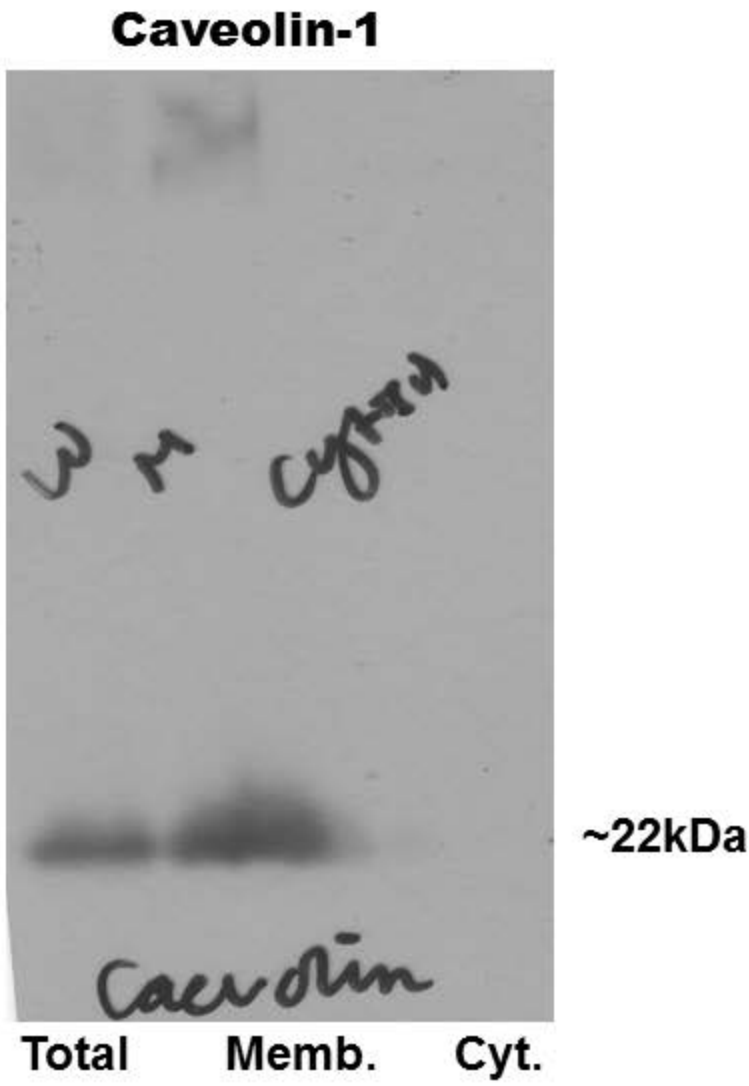

Figure 5B

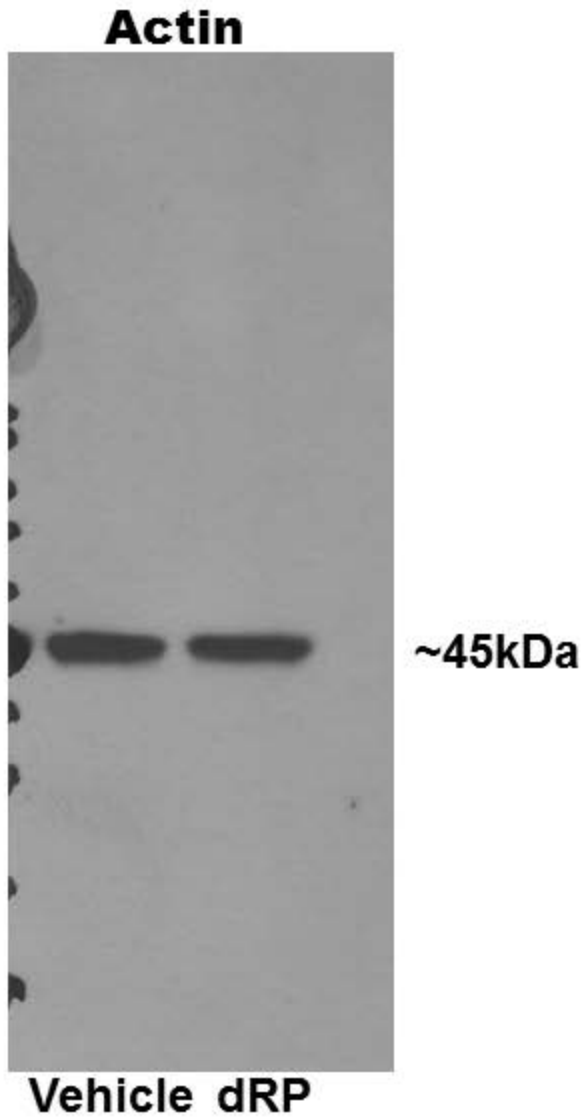

Figure 6

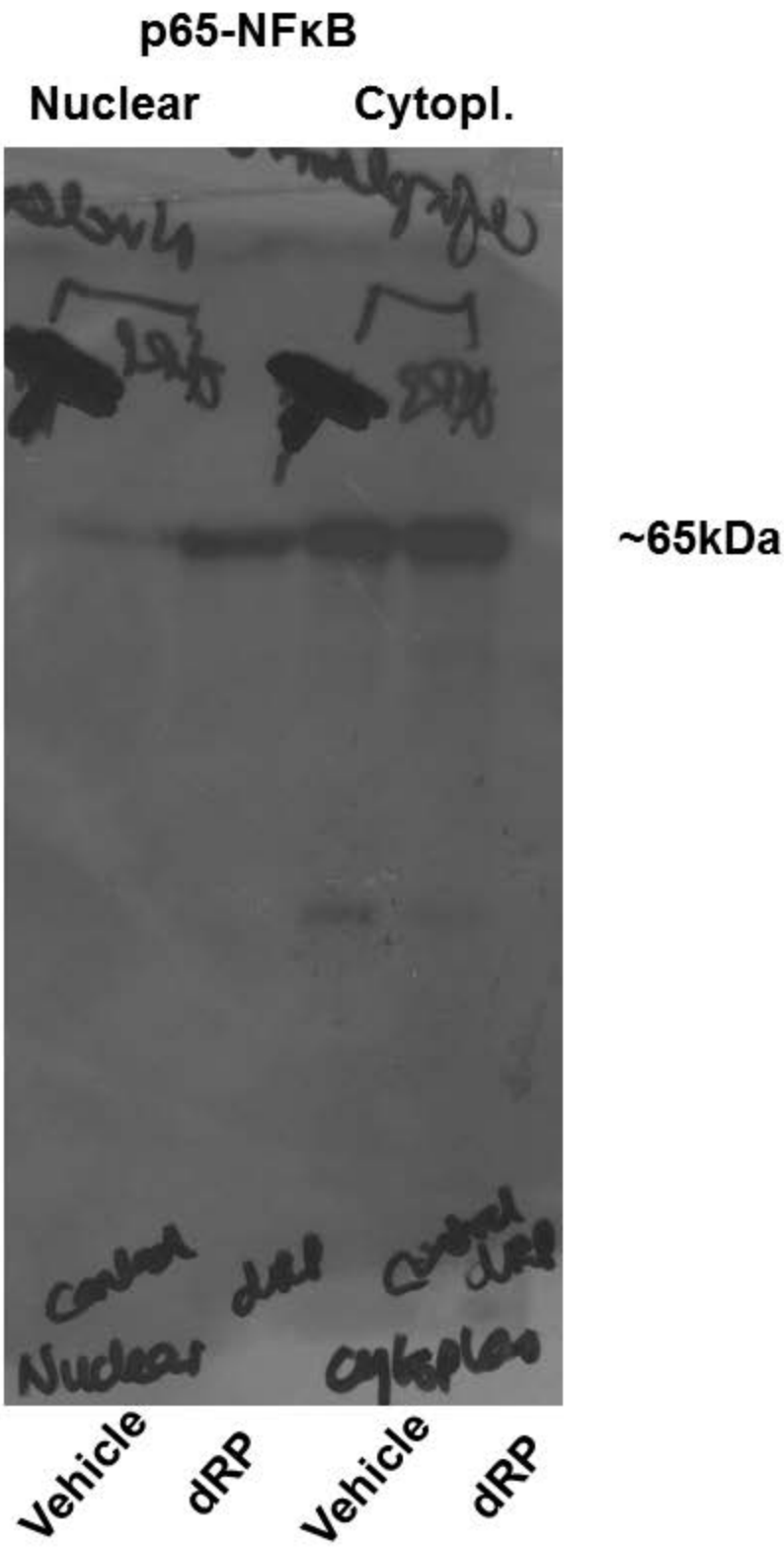

Figure 7B

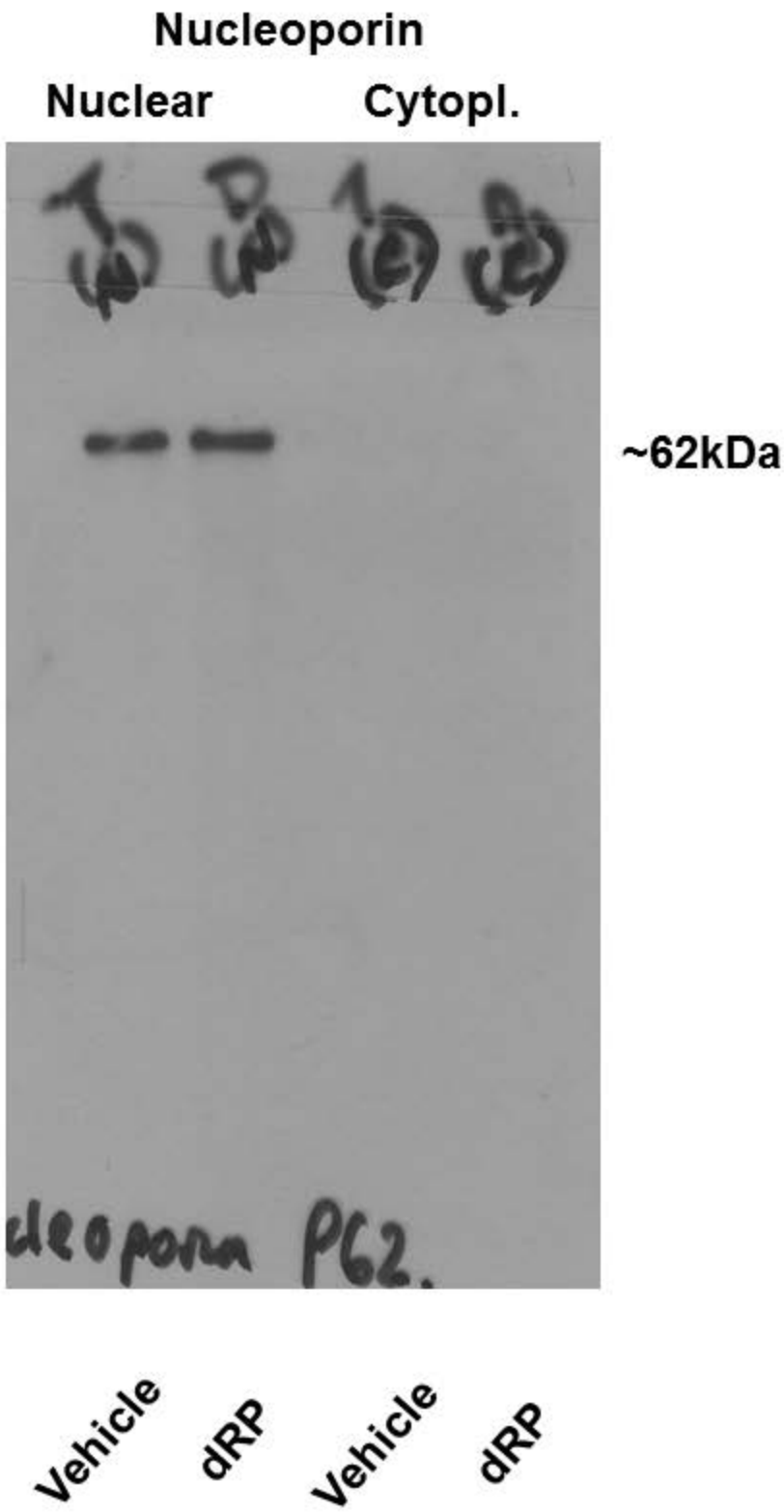

Figure 7B

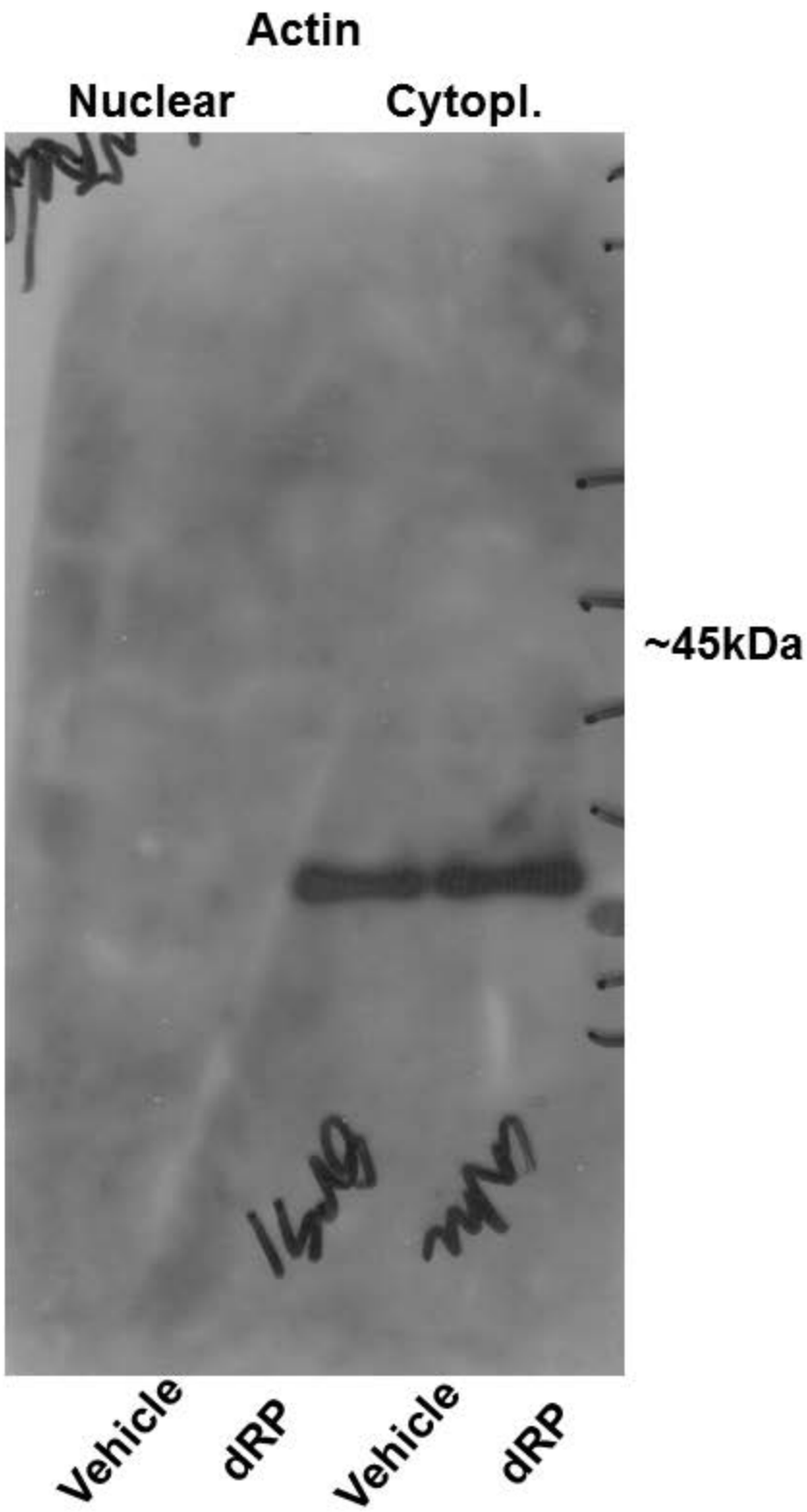

Figure 7B

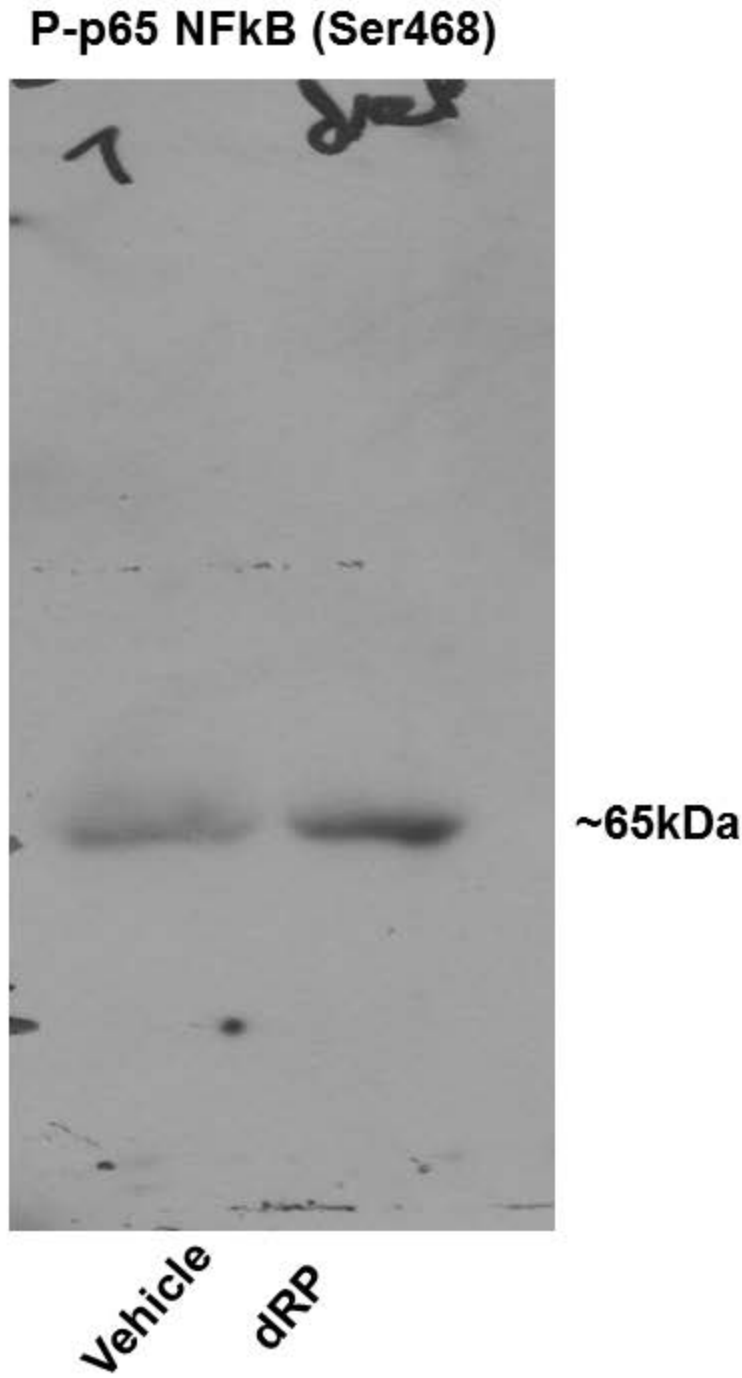

Figure 7C

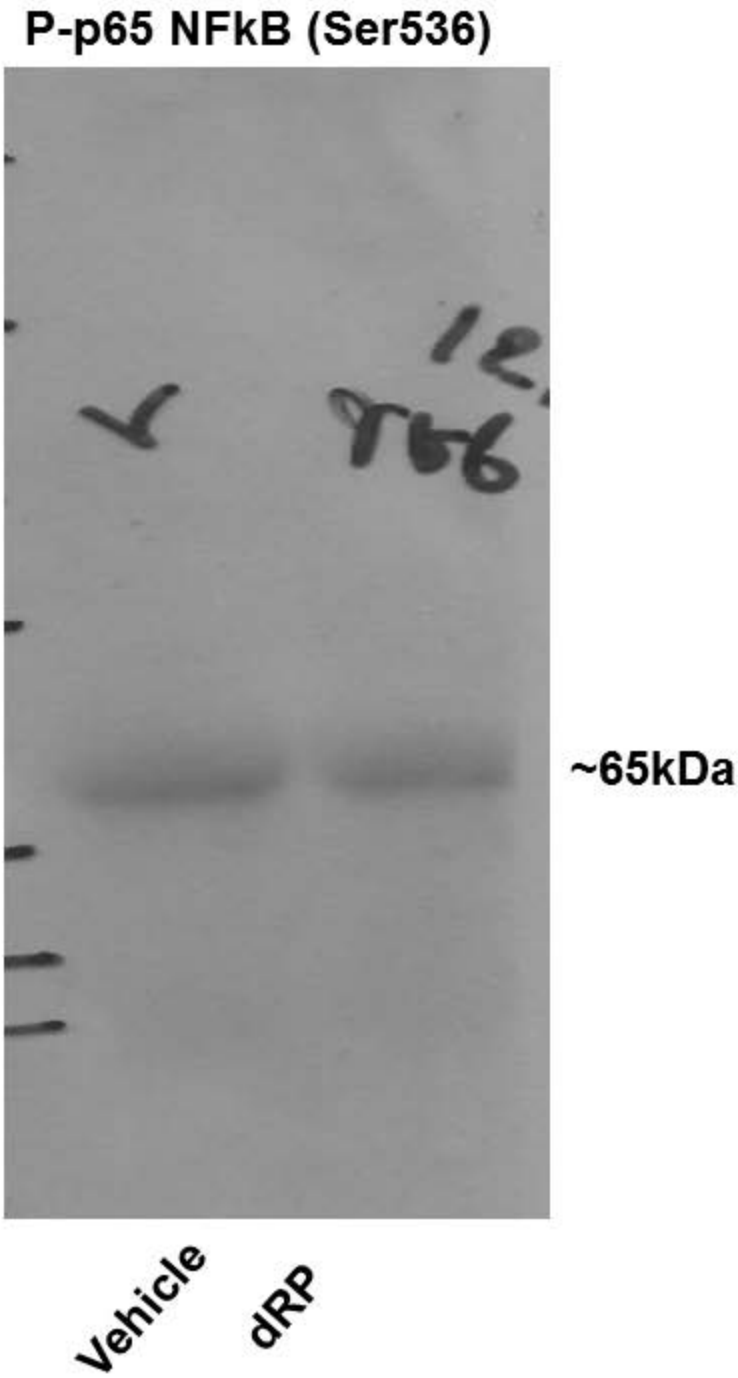

Figure 7C

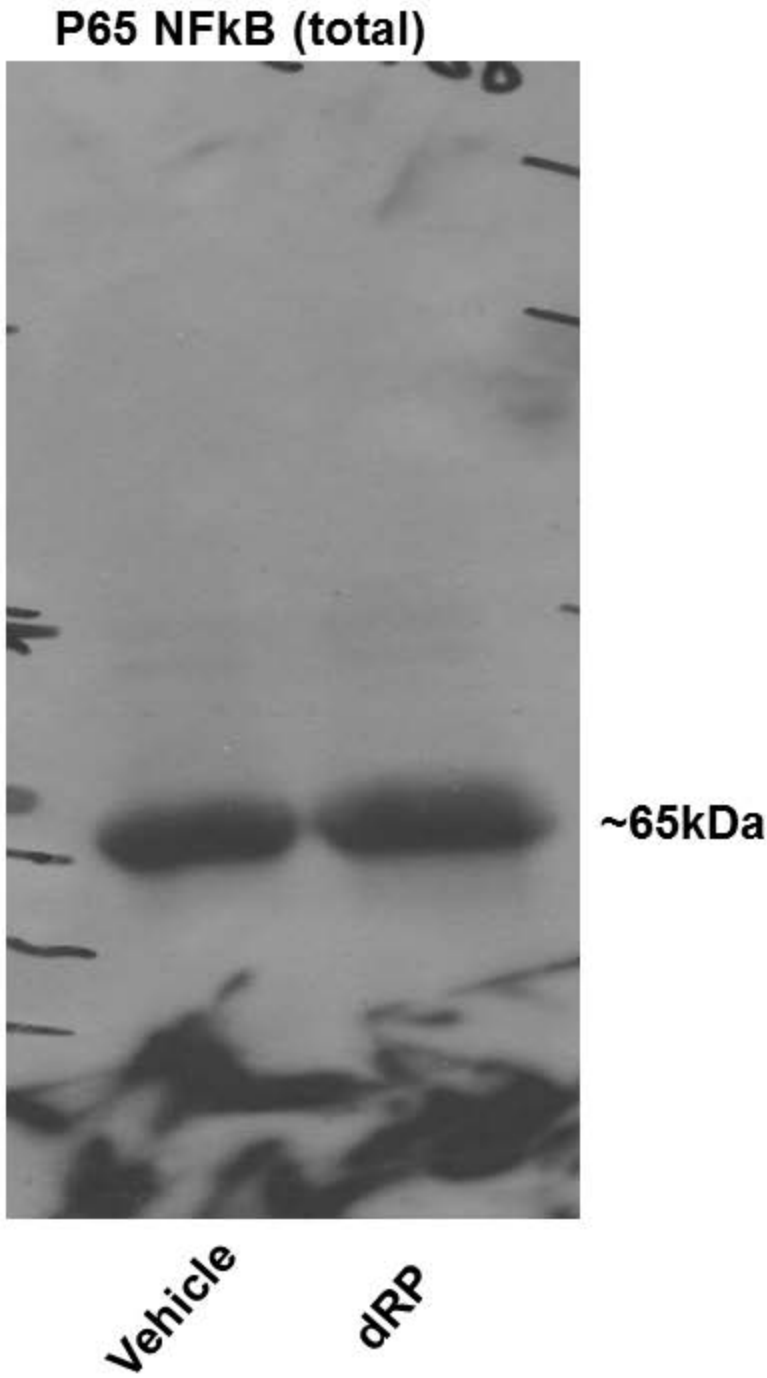

Figure 7C

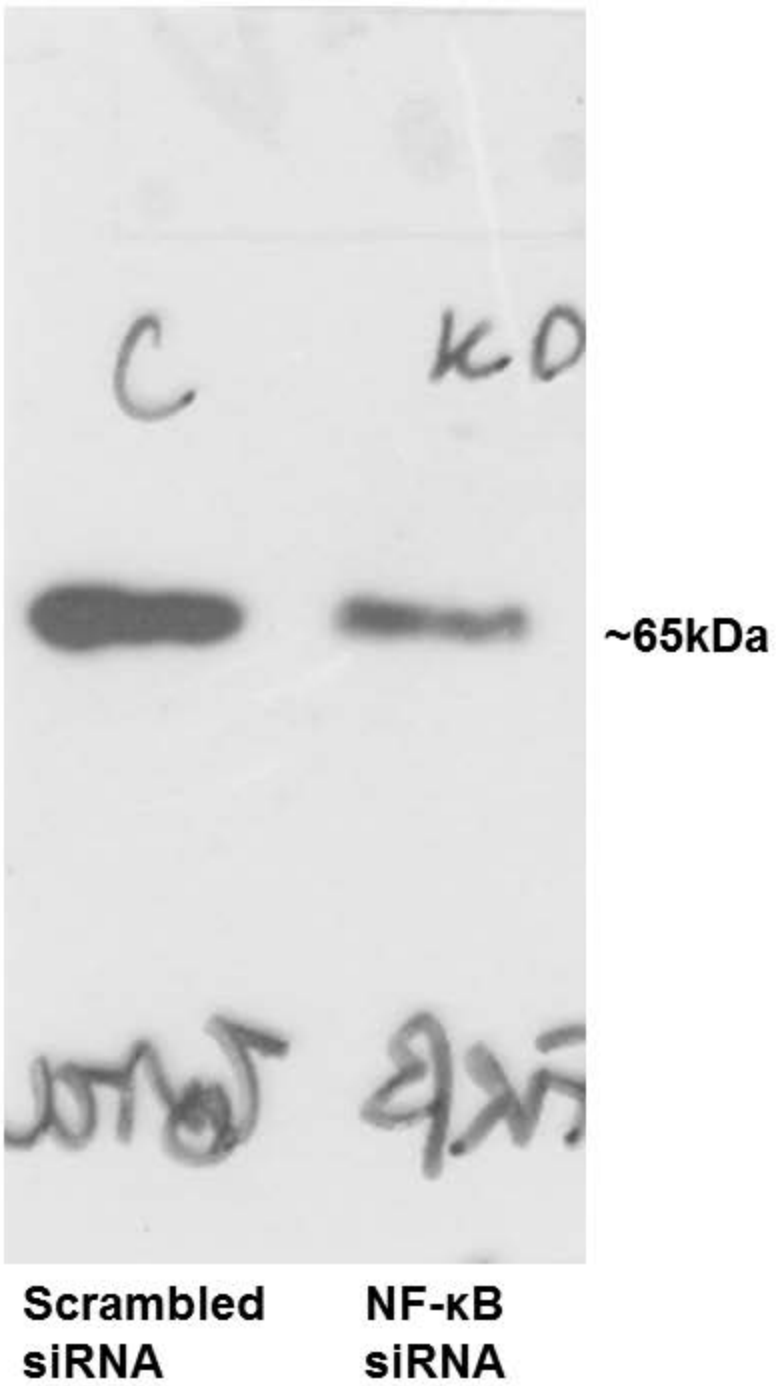

Figure 8B

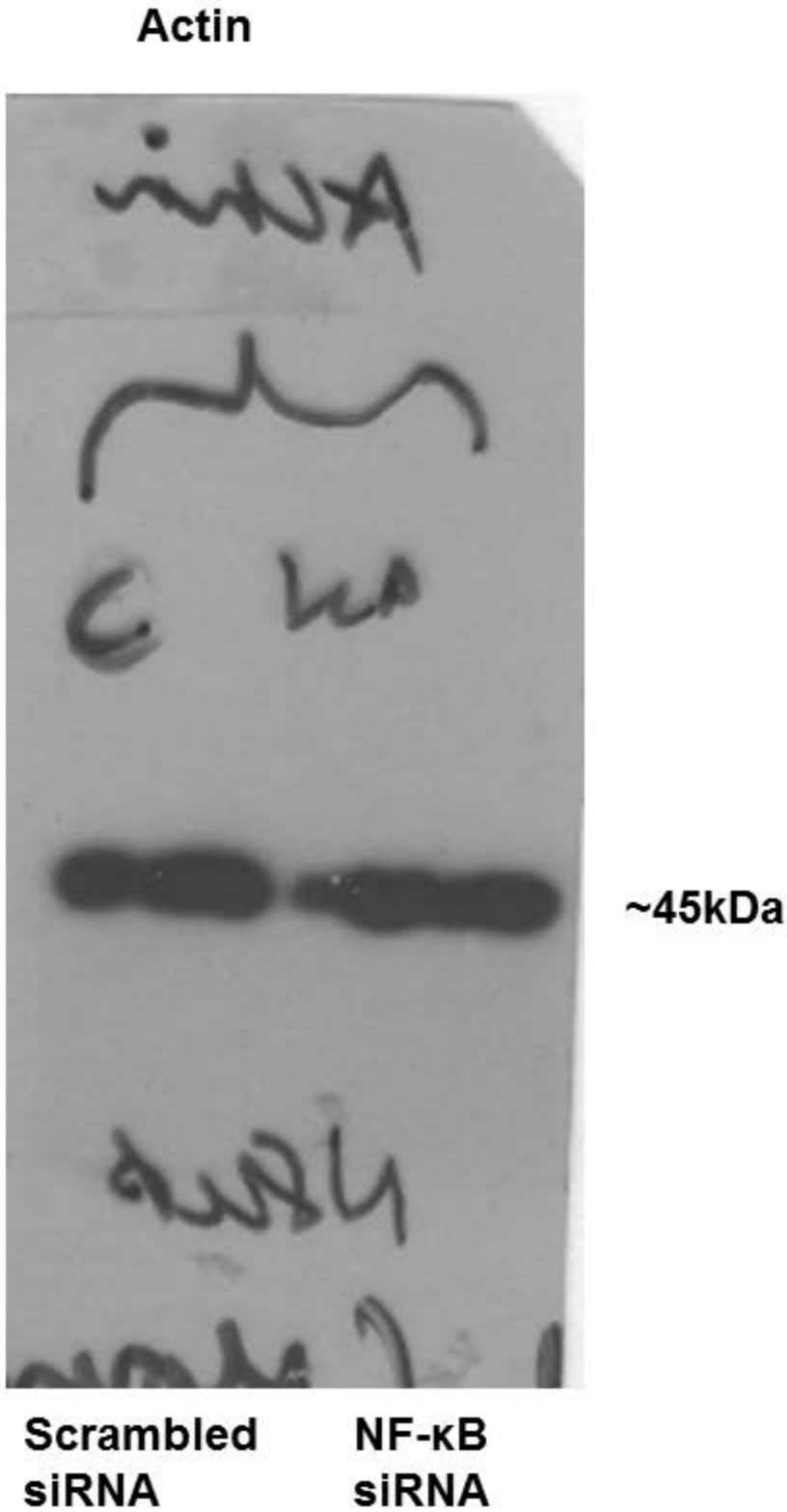

Figure 8B

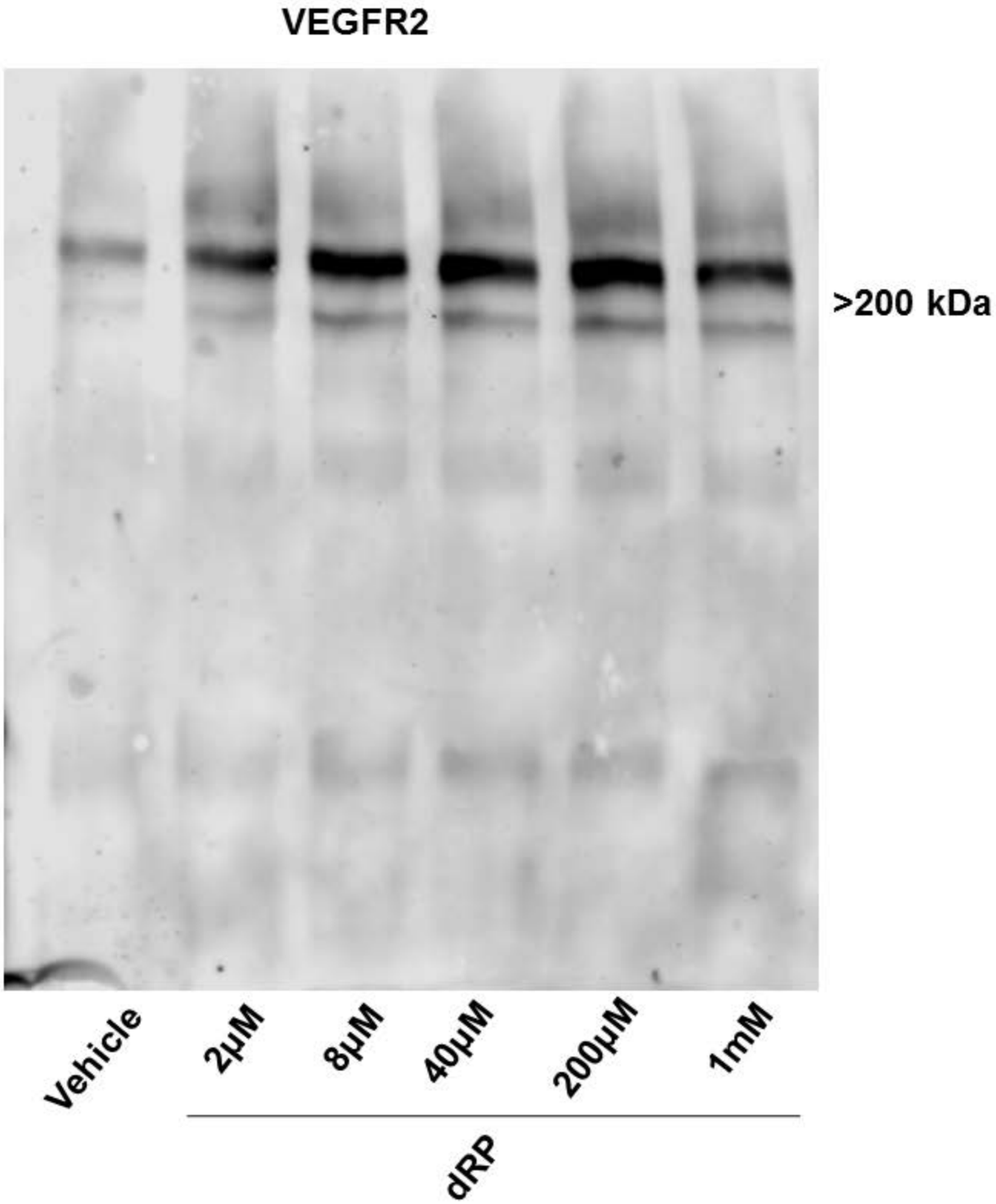

Figure 9B

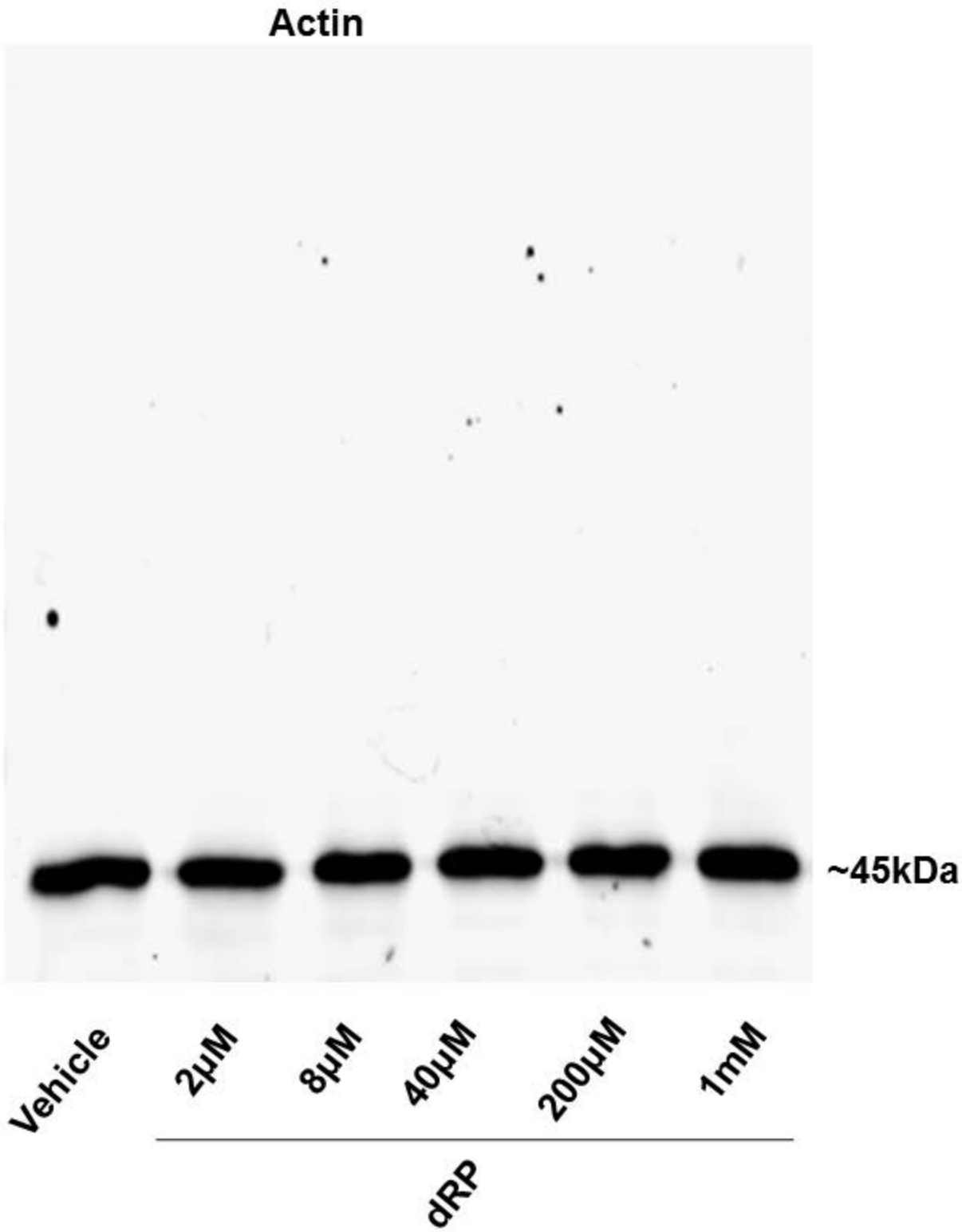

Figure 9B

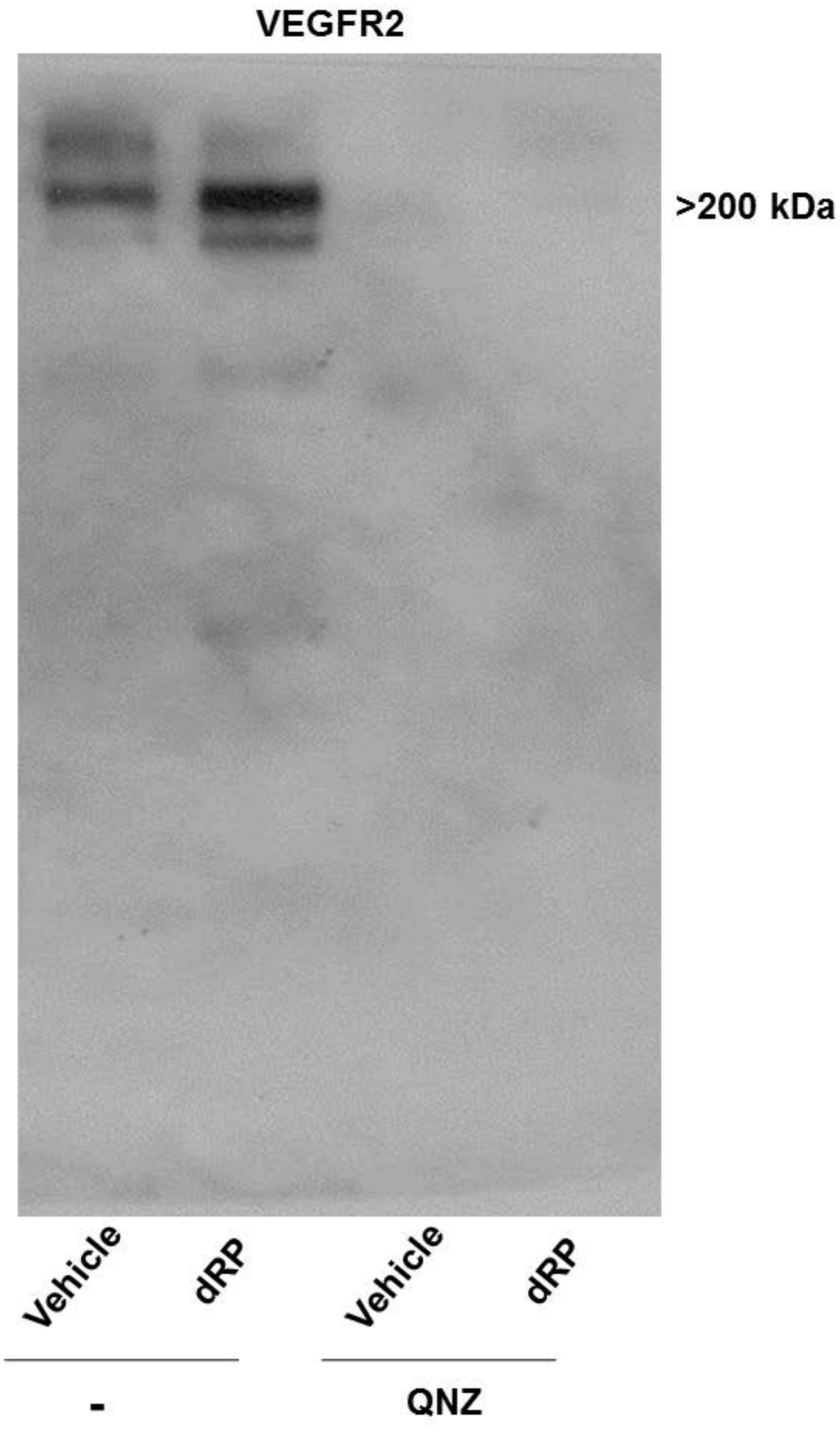

Figure 9C

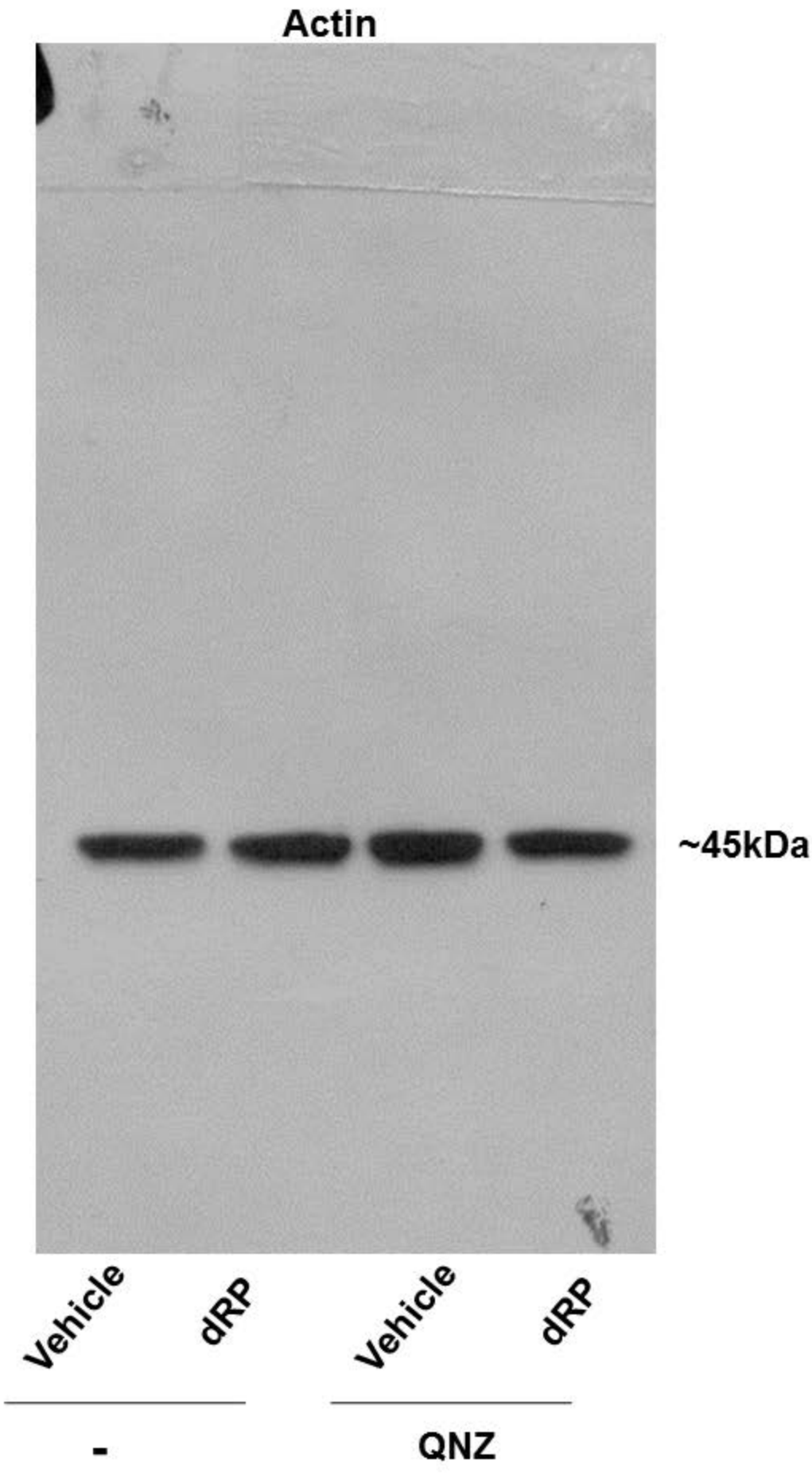

Figure 9C

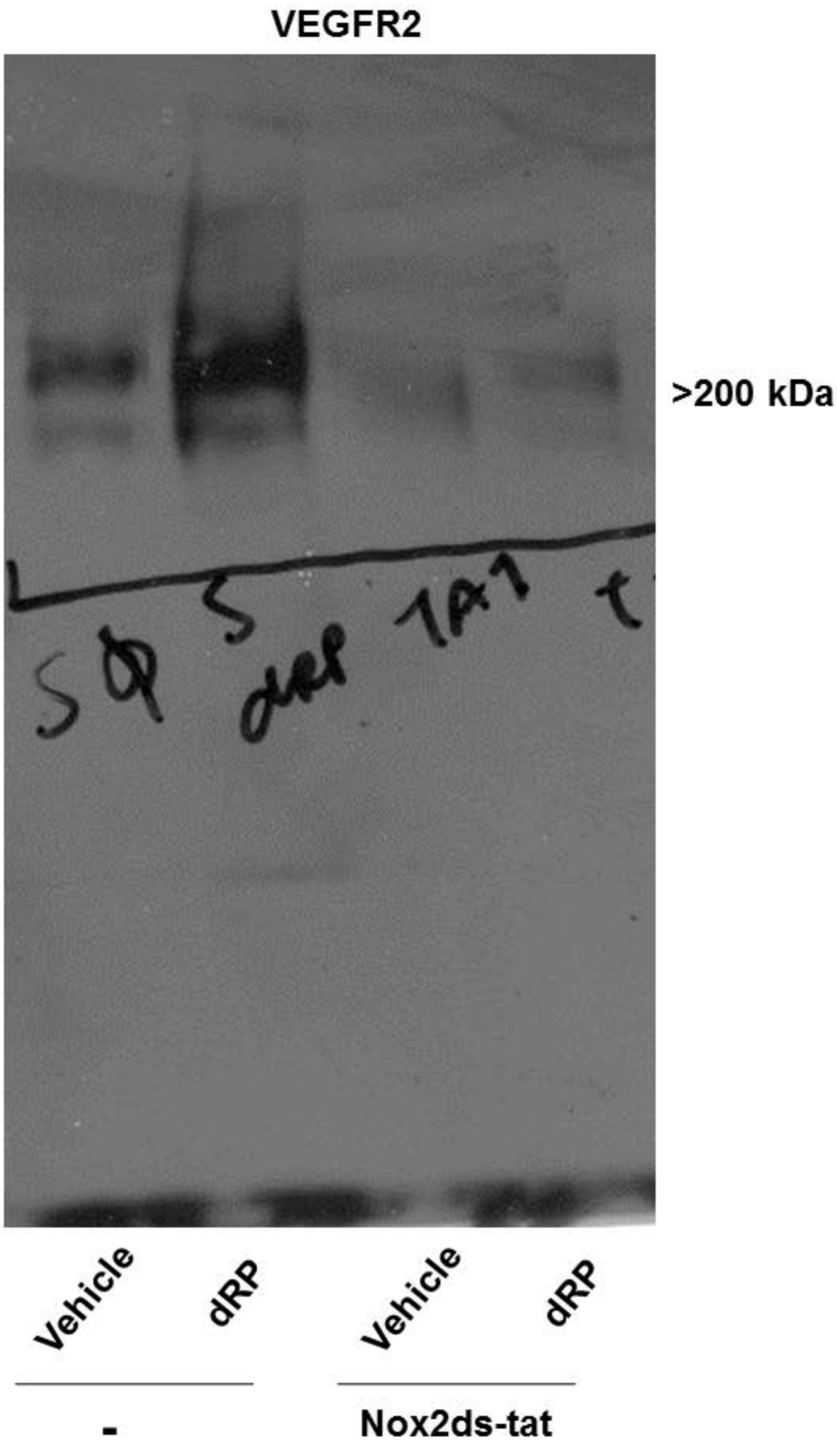

Figure 9D

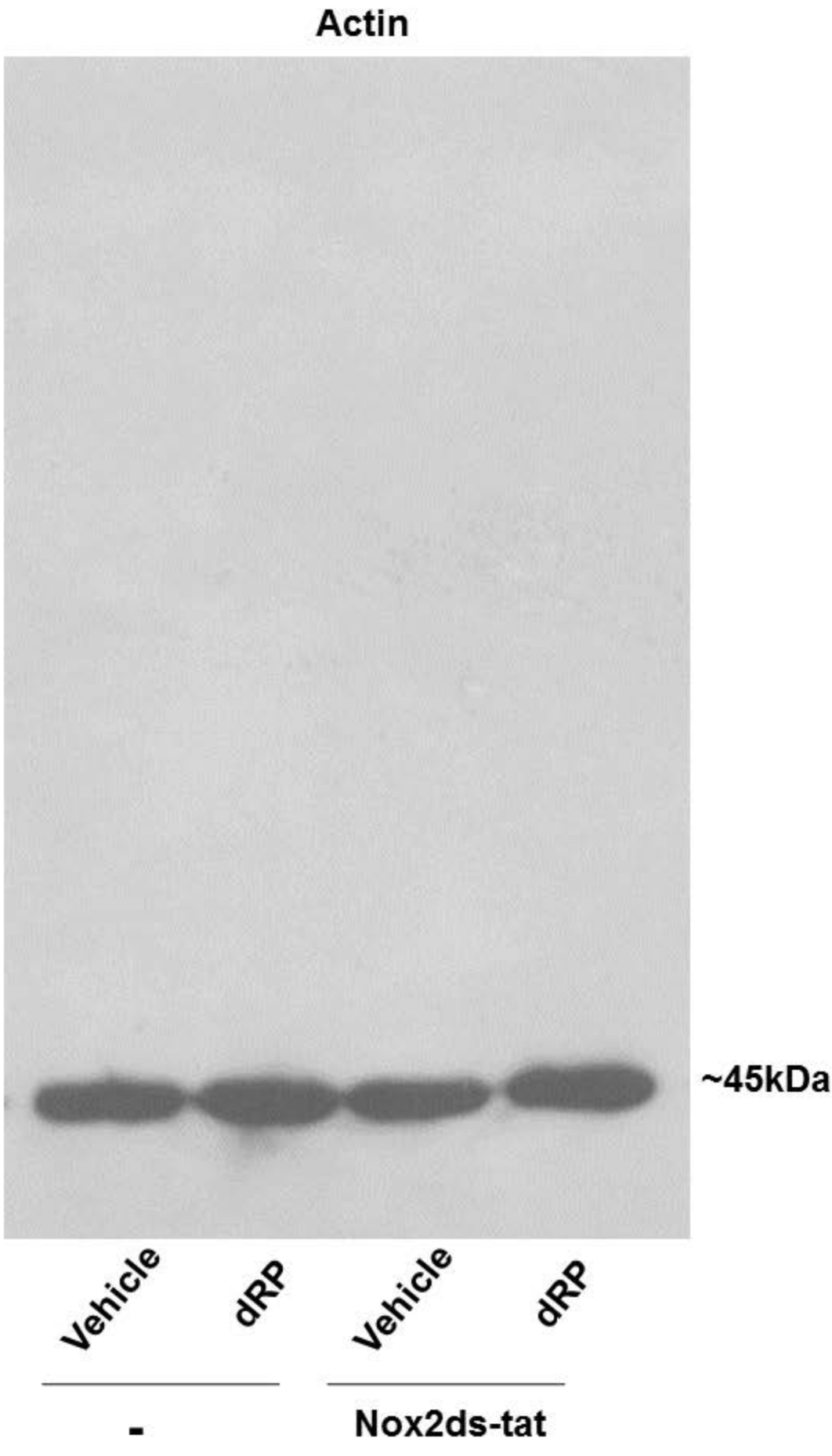

Figure 9D

FIGURE LEGENDS

Figure 1. dRP stimulates angiogenesis and oxidative stress of endothelial cells *in vitro*. (A) The concentration of dRP released by human platelets and mouse macrophages in vitro was quantified by LC-MS. Presented data are from 6 and 3 independent samples, respectively. Statistical significance was assessed by one-way ANOVA with Bonferroni post-hoc test (* = $p<0.01$ compared to non-stimulated platelets). (B-) HUVECs were seeded at a density of 3 x 10^2 cells/mm^2 on growth factor-reduced Matrigel® and cultured in basal medium (no FBS). Different concentrations of dRP between 2µM and 1mM and (after 4 hours of culture, quantification of tube number per optical field was performed using the Angiogenesis Analyzer plugin of ImageJ. (C) ROS generation was analysed with DHE staining for 1 hour in response to concentrations of dRP ranging from 2µM to 1mM and expressed as fold-increase over basal. (D) Time course of ROS generation in response to 200µM dRP in the presence of ROS scavengers 1mM NAC, 10µM MnTBAP or 10µM Tempol) or vehicle. ROS production was assessed after 5, 30, 60 and 120 minutes and expressed as fold-increase over basal. (E) HUVECs were seeded at a density of 3 x 10^2 cells/mm^2 on growth factor-reduced Matrigel® and cultured in basal medium (no FBS). 200µM dRP was incubated in the presence or absence of 1mM NAC, 10µM Tempol or 10µM MnTBAP. After 4 hours of culture, quantification of tube number per optical field was performed using the Angiogenesis Analyzer plugin of ImageJ. Representative pictures are shown in (i) and quantification is shown in (ii). Throughout the figure, data are expressed as mean ± SEM and analyzed by one-way ANOVA (B and C, n=6; E, n=8) or two-way ANOVA (D, n=6). In either case, Bonferroni post-hoc test was used to identify statistically significant difference between conditions; * = $p<0.05$ compared to vehicle, ** = $p<0.05$ compared to dRP). (E) Bars = 300µm.

Figure 2. dRP stimulates increased levels of ROS generation in HUVECs in a NOX-dependent manner. Quantitative measurements of superoxide anion production in HUVECs was performed using the cell-permeable superoxide-specific spin probe CMH and EPR. (A) Cells were treated for 45 minutes with 200μM dRP, vehicle (Tyrode's HEPES buffer) or 50ng/ml TNF-α in the presence of CMH (200μM) before EPR analysis. (B) Inhibition of superoxide anion production induced by 200μM dRP was also detected by EPR by 10μM MnTBAP, 10μM Tempol or 1μM VAS2870. For A and B, representative EPR traces are shown in (i). The bar charts in (ii) show superoxide anion production rates (pmol mg^{-1} min^{-1}) (mean ± SEM, one-way ANOVA with Bonferroni post-hoc test, * = $p<0.05$, n=4). (C) Calibration curve obtained using known concentrations of the oxidized spin probe (i.e. CM*). (D) Activation of NOX2 confirmed by co-immunoprecipitation with p47phox. HUVECs were treated with a vehicle or 200μM dRP for 1 hour. NOX2 immunoprecipitates were subjected to immunoblotting for p47phox and NOX2. Blots are representative of 4 independent experiments.

Figure 3. dRP stimulates increased levels of ROS generation and tube formation in a NOX-dependent manner. (A) ROS generation in response to 200μM dRP or vehicle was measured as described above in the presence of 1μM VAS2870. (B) dRP-induced ROS production resulted suppressed by inhibition of NOX2 with 10μM Nox2ds-tat. Immunoblot analysis of NOX2-specific knock down by siRNA (and scrambled siRNA control). (C) ROS generation in response to 200μM dRP was measured in control (scrambled siRNA) and NOX2 knockdown cells. (D) Representative images of tube formation by cells transfected with scrambled siRNA and NOX2 siRNA in the presence of 200μM dRP are shown. Total number of tubes was measured with the Angiogenesis Analyzer plugin of ImageJ. Representative images (top) and data analysis are shown (bottom). (E-F) Genetic silencing of NOX4 in HUVECs does not affect dRP-induced ROS generation increase. Tube formation in

response to 200µM dRP by scrambled and NOX4 knockdown cells was measured. Time courses in A, B , C and E were analysed by two-way ANOVA (n=4) with Bonferroni post-hoc test (* = $p<0.05$, compared to vehicle in A and B or vehicle/scrambled siRNA in C and E; ** = $p<0.05$ compared to dRP in A and B or dRP/scrambled siRNA in C and E). Bar graphs in D and F represent quantification of tube number per optical field compared by one-way ANOVA with Bonferroni post-test (* = $p<0.05$ compared to vehicle, n = 5). Bar: (D and F) 300µm.

Figure 4. dRP acts intracellularly following its internaliszation by the transporter GLUT1. (A) LC-MS detection of intracellular dRP. HUVECs were treated with 200µM dRP, before 3 washes in PBS and ultrasonication. Example chromatogram (upper panel) and data quantification (lower panel) are shown. Statistical significance was tested by t-test (* = $p<0.05$, compared to vehicle, n=4). (B) STF-31 and fasentin (10µM) inhibited dRP- but not VEGF-dependent tube formation. Example pictures (upper panel) and data quantification (lower panel) are shown. Bar graphs represent quantification of tube number per optical field compared by one-way ANOVA with Bonferroni post-hoc test (* = $p<0.05$ compared to vehicle, n = 5). Bar: 300µm. (C) siRNA-dependent silencing of GLUT1 inhibits dRP-induced ROS generation. Following GLUT1 silencing displayed in top panels, ROS was measured as described over a period of two hours. Time courses were analysed by two-way ANOVA (n=4) with Bonferroni post-hoc test (* = $p<0.05$, compared to vehicle/scrambled siRNA; ** = $p<0.05$ compared to dRP/scrambled siRNA). (D) siRNA-dependent silencing of GLUT1 inhibits dRP-induced tube formation. Example pictures for dRP response by HUVECs treated with scrambled siRNA or GLUT1 siRNA are shown in top panels. Bar graphs represent quantification of tube number per optical field compared by one-way ANOVA with Bonferroni post-hoc test (* = $p<0.05$ compared to scrambled siRNA/vehicle, ** = $p<0.05$ compared to scrambled siRNA/dRP, ns = non significant, n = 4). Bar: 300µm.

Figure 5. dRP directly activates NOX2. (A) Binding of NOX2 was assessed by pull-down using a mixture of three dRP-biotin conjugates (i). NOX 1, 2, 4, and actin were detected by immunoblotting (ii) (4 independent experiments). (B) Membrane fractions treated with dRP display NOX activation. NOX-1, 2, 4, Caveolin-1 and β-actin were tested by immunoblotting (i). The membrane fractions were treated with 200μM dRP using cytochrome c reduction assay. Cytochrome c reduction was measured as absorbance at wavelength 550nm. 1000 U/mL SOD was utilized to determine the superoxide anion-dependent component, while DPI (100μM) was used to determine the role of NOXs and other flavoenzymes (ii). 10μM Nox2ds-tat (or scrambled peptide as a negative control) was utilised to assess the role of NOX2 in the oxidative response measured by this membrane assay (iii). Data in B were analysed by one-way ANOVA with Bonferroni post-test (* = $p<0.05$, compared to vehicle (ii) or scrambled siRNA/vehicle (iii), ** = $p<0.05$ compared to dRP (ii) or scrambled siRNA/dRP (iii), n=6).

Figure 6. dRP induces oxidative stress without significantly increasing apoptosis. (A) HUVECs treated with or without 200μM dRP for 4 hours were labelled for 2 h with 20μM BIAM in anoxic conditions. Thiol oxidation status was determined by protein separation using SDS-PAGE and staining with HRP-streptavidin. Green arrows indicate thiol oxidation, whilst red arrows represent thiol reduction. β-actin immunoblotting was used to confirm equal loading. Blots are representative of 4 independent experiments. (B) VitaBright-43® staining was also utilized to measure the level of intracellular reduced thiols. HUVECs were treated with vehicle solution (Tyrode's HEPES buffer) or stimuli with/without NOX inhibitor (200μM dRP, 10μM DPI) for 30 min. Cells were co-stained with VitaBright-43® and propidium iodide and analysed by image cytometry using the NucleoCounter NC-3000® system. Plots show VitaBright-43® (VB) intensity versus propidium iodide intensity are shown (i). Intracellular thiol oxidation was quantified by counting the % of cells with

VitaBright-43® staining below 10,000 rfu (ii). Statistical analysis was performed by one-way ANOVA with Bonferroni post-test (* = $p<0.05$, compared to vehicle, n=6). (B Cell apoptosis was measured by flow cytometry for PE-annexin V staining. HUVECs were treated with vehicle (Tyrode's HEPES buffer), 200μM dRP or 5mM diethyl maleate (positive control) for 12 h. Forward scattering (FSC)/side scattering (SSC) and annexin V staining histograms from 4 independent experiments are presented (i). Data analysis is also shown (ii). Data are mean ± SEM analyzed by one-way ANOVA with Bonferroni post-test (* = $p<0.05$, compared to vehicle, n=6).

Figure 7. NF-κB is activated in response to dRP. (A) DNA-binding capacity of NF-κB (p65 subunit) was determined using TransAM® for NF-κB (Active Motif, cat. no. #43296). HUVECs were treated with or without 200μM dRP for 30 minutes. Whole cell extract from Jurkat cells stimulated with 12-*O*-tetradecanoylphorbol-13-acetate and calcium was used as positive control. One-way ANOVA with Bonferroni post-test was used to test statistical significance (mean ± SEM, n=6, * = $p<0.05$). (B) The translocation of p65-NF-κB to the nucleus was tested by subcellular fractionation using the NE-PER kit (Pierce). Cytoplasmic and nuclear fractions were immunoblotted for p65-NF-κB, nucleoporing-p62 (a nuclear marker) and β-actin (a cytoplasmic marker). Data are representative of 4 independent experiments. (C) NF-κB activation was also investigated by phospho-specific immunoblotting. Total cell lysate immunoblotted with phospho-specific NF-κB antibodies (Ser468 or Ser536) and total NF-κB antibody (as loading control). Immunoblots represent 4 independent experiments. (D) Immunolocalisation of p65-NF-κB (green) in dRP-stimulated HUVECs (200μM, 1 hour) was also tested. Where indicated, 100nM QNZ, an inhibitor of NF-κB activation, was added. 100μM DPI was used as a NOX inhibitor, whereas 50 ng/ml TNF-α was utilized as a positive control. Images are representative of 5 independent experiments. Bar: (D) 100μm.

Figure 8. dRP induces NF-κB activation in a NOX-dependent manner and NF-κB activity is critical for endothelial tube formation in response to dRP. (A) Representative immunofluorescence images of HUVECs stained for NF-κB (green) and DAPI (blue). Where indicated, HUVECs were pre-treated with 10μM Nox2ds-tat peptide for 1 hour or subjected to NOX2 and p22phox siRNA-mediated genetic silencing for 72 h prior to treatment with 200μM dRP for 30 minutes. Images are representative of 4 independent experiments. (B) Tube formation was assessed by seeding scrambled and NF-κB siRNA-treated cells onto growth factor-reduced Matrigel® with or without 200μM dRP. Representative images show tube formation after 4 hours (left) and p65-NF-κB downregulation (right). Bar graphs (bottom right) represent quantification of tube number per optical field using ImageJ software with Angiogenesis Analyzer plugin (* = $p<0.05$, one-way ANOVA with Bonferroni post-test, n = 5). Bar: (A) 100μm; (B) 300μm.

Figure 9. VEGFR2 is upregulated in response to dRP in a NF-κB-dependent manner and its activity is necessary for dRP-dependent angiogenesis. (A) qPCR analysis of VEGFR2 expression on HUVECs treated with or without 200μM dRP for 4 hours. The $2^{-\Delta\Delta Ct}$ analysis method was used to analyse the data with GAPDH used as normalizer. Statistical significance of the difference was tested using non-parametric Mann-Whitney test (mean ± SEM, n=4, * = $p<0.05$). (B) HUVECs were treated with increasing concentration of dRP (2μM to 1mM) for 6 hours. Alternatively, HUVEC were incubated with (C) 100nM QNZ or (D) 10μM Nox2ds-tat for 1 hour and then stimulated with 200μM dRP for 6 hours. Cell lysates were immunoblotted for VEGFR2 and β-actin. Data are representative of 4 independent experiments. (E) Effects of VEGFR2 inhibitors Pazopanib and mAB3572 on dRP-induced tube formation. HUVECs with or without 200μM dRP were tested in the presence of 10 μg/ml Pazopanib and 50 ng/mL mAB3572 antibody. Representative pictures in (i) and quantification in (ii). (F) Effects of the NF-κB inhibitor QNZ (100nM) on dRP-

induced tube formation. Representative pictures in (i) and quantification in (ii). Bar graphs represent quantification of tube number per optical field performed using ImageJ software with Angiogenesis Analyzer plugin and compared by one-way ANOVA with Bonferroni post-test (* = $p<0.05$, n=6). Bar: (E and F) 300µm.

Figure 10. dRP stimulates VEGFR2 upregulation and NOX2-deoendent angiogenesis *in vivo*. (A) Representative examples (i) and quantification (ii) of the hematoxylin/eosin staining of wound tissue treated with dRP or vehicle control (PBS). Data represent counts of vascular structures (surrounded by continuous intimal monolayer) per optic field. Statistical significance of the difference was assessed by non-parametric Mann-Whitney test (* = $p<0.05$ compared to vehicle, n = 10). Vascular structures are highlighted by white arrows in the picture. (B) Representative examples (i) and quantification (ii) of the VEGFR2-specific staining of wound tissue treated with dRP or vehicle control (PBS). Data represent counts of high fluorescence intensity areas per mm^2, as estimated using ImageJ. Statistical significance of the difference was assessed by non-parametric Mann-Whitney test (* = $p<0.05$ compared to vehicle, n = 8). (C) Representative examples (i) and quantification (ii) of the hematoxylin staining of Matrigel™ plugs containing dRP (41.2µg/plug) or vehicle control (PBS) after 7 days of implantation in wild type (C57BL6/J) or $NOX2^{-/-}$ (Jackson Laboratories B6.129S-Cybbtm1Din/J) mice. Data represent counts of capillary structures per mm^2, as estimated using ImageJ. Statistical significance of the difference was assessed by one-way ANOVA with Bonferroni post-hoc test (* = $p<0.05$ compared to vehicle, ** = $p<0.05$ compared to dRP, n=6). (D) Representative examples (i) and quantification (ii) of the DAPI/CD31-specific staining of Matrigel™ plugs containing dRP (41.2µg/plug) or vehicle control (PBS) after 7 days of implantation in wild type (C57BL6/J) or $NOX2^{-/-}$ (Jackson Laboratories B6.129S-Cybbtm1Din/J) mice. Data represent counts of capillary structures per mm^2, as estimated using ImageJ. Statistical significance of the difference was assessed by one-way

ANOVA with Bonferroni post-hoc test (* = $p<0.05$ compared to vehicle, ** = $p<0.05$ compared to dRP, n=6).Bars: 300µm (throughout).